

Master-thesis

**Influence of oxygen stoichiometry onto
physical properties of $\text{La}_{0.7}\text{Sr}_{0.3}\text{MnO}_{3-\delta}$
powder and thin films**

by Hengbo Zhang

of Material Science in RWTH Aachen

November 2020

supervised by

Prof. Dr. Thomas Brückel

Prof. Dr. Regina Dittmann

PD Dr. Oleg Petravic

at JCNS-2/ PGI-4, Forschungszentrum Jülich GmbH

Zusammenfassung

Sauerstofffehlstellen spielen eine entscheidende Rolle bei der Kontrolle der physikalischen Eigenschaften von komplexen Oxiden. Die Gitter-Struktur und insbesondere die magnetischen und elektrischen Transporteigenschaften können durch einen Postannealing-Prozess modifiziert werden. Der entscheidende Parameter ist hierbei die Sauerstoff-Stöchiometrie. Dies bietet zahlreiche Möglichkeiten für technologische Anwendungen, z.B. in der Informations-Verarbeitung, Katalyse oder Sensorik.

In dieser Arbeit wurden $\text{La}_{0.7}\text{Sr}_{0.3}\text{MnO}_3$ (LSMO) Dünnschichten mittels Hochdruck-Sauerstoff Sputtern bei 2mbar Sauerstoff-Partialdruck auf SrTiO_3 (STO) Einkristall-Substraten aufgewachsen. Danach wurden die Struktur und die physikalischen Eigenschaften von so hergestellten LSMO Dünnschichten mit unterschiedlichen Dicken charakterisiert. Alle Dünnschichten befinden sich in der Perowskit-Phase mit demselben Gitterparameter und zeigen ein typisches ferromagnetisches Verhalten mit ähnlichen Koerzitivfeldstärken, Sättigungsmagnetisierungen und Curie-Temperaturen. Mit einem XMCD-Spektrum und polarisierter Neutronen-Reflektivität an einer LSMO-Dünnschichtprobe kann gezeigt werden, dass die Probe ferromagnetisch ist und die Magnetisierung mit den makroskopischen Magnetisierungsmessungen vergleichbar ist.

Nach der Charakterisierung der Dünnschichten wurden verschiedene Postannealing-Prozesse angewendet, z.B. Hochvakuum (HV), Ultrahochvakuum (UHV) und Aluminium (Al) unterstütztes Postannealing, um den Phasenübergang von Perowskit (PV) zu Brownmillerit (BM) in LSMO-Dünnschichten auszulösen. Im Vergleich zum HV-Postannealing, kann eine reinere BM-Phase mit geringerer Magnetisierung durch UHV-Postannealing erzeugt werden. Das Mn-XMCD Spektrum bestätigt keine Nettomagnetisierung nach dem Postannealing, was durch die Erhöhung des Anteils an Mn^{2+} Valenz im System erklärt werden kann. Außerdem wurden die Dünnschicht-Proben zusammen mit poliertem Aluminium 15 Stunden bei 300°C getempert. Aus dem XRD- und RBS-Spektrum geht jedoch hervor, dass die LSMO-Struktur vollständig zerstört wurde, was darauf hinweist, dass dieses Al-unterstütztes Postannealing Verfahren für Dünnschichten zu reduktiv ist.

Zusätzlich wurde der Phasenübergang von LSMO-Pulvern untersucht. Das Ziel ist es, das spannungsfreie Bulk-system mit dem verspannten epitaktischen Filmsystem zu vergleichen. Durch

Postannealing wurde der Phasenübergang von PV zu BM ebenfalls erfolgreich ausgelöst. Die magnetischen und elektronischen Transporteigenschaften zeigen den Übergang vom ferro- zum antiferromagnetischen und vom leitenden zum isolierenden Verhalten.

Abstract

Oxygen vacancies play a crucial role for controlling physical properties in complex oxides. The oxygen stoichiometry can be tuned e.g. via absorbing or desorbing oxygen and by this modifying the lattice structure, magnetic and electronic transport properties. This provides the possibility for technological applications, e.g. in information storage, catalysis or sensorics.

In a previous study, the optimal growth parameters are found for $\text{La}_{0.7}\text{Sr}_{0.3}\text{MnO}_3$ (LSMO) thin films grown on SrTiO_3 (STO) single crystal substrates by using High Oxygen Pressure Sputter Deposition (HOPSD). In this study, the physical properties of as-prepared LSMO thin films with different thickness are characterized. All the samples are in the Perovskite phase with the same out-of-plane lattice parameter and show a typical ferromagnetic behaviour with similar coercive fields, saturation magnetizations and Curie temperatures. From a XMCD spectrum and polarized neutron reflectivity results on an as-prepared sample it is exemplarily shown that the samples are ferromagnetic, and the magnetization is comparable to the macroscopic magnetization measurement.

After characterization of the as-prepared samples, various annealing methods are applied to trigger the phase transition of LSMO thin films. In the previous study, the phase transition from Perovskite (PV) to Brownmillerite (BM) is triggered successfully by high vacuum (HV) annealing [1]. Here the samples are annealed using different methods, i.e. ultra-high vacuum annealing (UHV) and Aluminum (Al) assisted annealing. The previous HV annealing method is also repeated for comparison. In this study, a purer BM phase sample with less magnetization is obtained by UHV annealing. The Mn XMCD spectrum confirms no net magnetization in the annealed system, which can be explained by the increase of the amount of Mn^{2+} valency in the system. Moreover, the thin film samples are also annealed together with polished Aluminum at 300°C for 15 hours. However, from the XRD and RBS results, it is found that the LSMO structure is completely destroyed, indicating that this method is too reductive for thin films.

In addition, the phase transition of LSMO powder is studied. The powder represents a bulk system. The aim is to compare the strain free bulk system with the strained epitaxial film system. The PV to BM phase transition is also successfully triggered. The magnetic and electronic transport results support the transition from ferro- to anti-ferromagnetic and from conducting to insulating behavior.

Contents

1	Introduction	1
2	Theoretical background	2
2.1	Perovskite structure variants	2
2.1.1	Perovskite (ABO_3)	2
2.1.2	Brownmillerite ($ABO_{2.5}$)	3
2.2	Transition metal oxides	4
2.2.1	$La_xSr_{1-x}MnO_3$	4
2.3	Magnetism in transition metal oxides	6
2.3.1	Electronic structure	6
2.3.2	Exchange interactions	8
2.3.3	Mean Field Theory (MFT) Approximation for a ferromagnet	9
2.4	Thin film growth	11
2.4.1	Growth methods	11
2.4.2	Growth modes	12
2.5	Scattering theory	13
2.5.1	X-Ray diffractometry (XRD)	14
2.5.2	X-Ray reflectometry (XRR)	14
2.5.3	Reciprocal space mapping (RSM)	15
2.5.4	Polarized neutron reflectometry (PNR)	17
3	Experimental methods and instruments	21
3.1	High Oxygen Pressure Sputtering Deposition (HOPSD)	21
3.2	X-Ray Reflectometry/ Diffractometry (XRR and XRD)	22

3.3	SQUID magnetometry (MPMS)	23
3.4	Physical Properties Measurement System (PPMS).....	24
3.5	Polarized Neutron Reflectometry (PNR).....	25
3.6	Rutherford Backscattering Spectrometry (RBS)	26
3.7	X-ray Absorption Spectroscopy and X-Ray Magnetic Circular Dichroism (XAS and XMCD).....	27
4	Structural and physical properties of as-prepared LSMO thin films.....	29
4.1	Sample preparation	29
4.1.1	Substrate Selection.....	29
4.1.2	Growth parameters.....	30
4.1.3	Stoichiometry of the as-prepared samples	31
4.2	Thickness dependent physical properties change on LSMO thin films..	33
4.2.1	Structure	33
4.2.2	Magnetization	34
4.2.3	Mean Field Theory Approximation fitting for as-prepared sample 36	
4.2.4	Polarized Neutron Reflectometry on as-prepared system	38
5	Control of physical properties via topotactic phase transition on LSMO thin films by post-annealing.....	41
5.1	Annealing methods	41
5.2	Structural changes induced by post-annealing.....	41
5.3	Physical property changes after post-annealing.....	45
5.3.1	Magnetometry.....	45
5.3.2	Resistivity	49

5.3.3	Optical Property	50
5.4	Peak oscillation phenomena during vacuum annealing	50
5.5	Summary	53
6	Control of physical properties via topotactic phase transition on LSMO powders by post-annealing	55
6.1	Powder sample preparation	55
6.2	Topotactic phase transition induced by Aluminum-assisted annealing ..	56
6.3	Magnetic and electronic transport properties change.....	58
6.4	Summary	60
	Summary & Outlook	61
	Acknowledgement.....	63
	References.....	64

1 Introduction

The influence of oxygen vacancies in complex transition metal oxides is currently intensely investigated because of its strong influence onto the physical properties of the oxides, i.e. onto the lattice structure, electronic transport and magnetic behavior. The controlled tunability of the properties via oxygen absorption or desorption provides the possibility for applications in e.g. information storage technology, chemical catalysis and sensors.

In this study, the transition metal oxide $\text{La}_x\text{Sr}_{1-x}\text{MnO}_3$ (LSMO) is selected due to its controllable crystallographic structure and accordingly changeable magnetic and electrical properties during the absorption or desorption of oxygen. Through oxygen desorption a Brownmillerite phase (BM) can be achieved from the initial Perovskite phase (PV) by vacuum annealing. During this process the valency of the transition metal cation is changed, leading to a different electronic behavior resulting in different physical properties, e.g. ferromagnetic versus antiferromagnetic behavior and metallic versus insulating behavior.

For the preparation of the thin films, High Oxygen Pressure Sputter Deposition (HOPSD) is chosen because of the flexibility to control the growth parameters in a wide range. For the bulk system, the powder sample is obtained by hand-milling from the LSMO target. After preparation, the PV to BM phase transition is triggered on both thin film and powder system. Then the physical properties changes between various annealing methods and different systems are compared.

Outline of this thesis

In Chapter 2 the scientific background of magnetism, lattice structure, scattering theory and the physical properties of the investigated system (LSMO) are introduced. Then the experimental methods and instruments used for the characterization of the thin films and powder are illustrated in Chapter 3. The physical properties of as-prepared LSMO thin films are discussed in Chapter 4. Chapter 5 introduces the structural, magnetic and electronic properties changes on thin films after various annealing methods. Next, the post-annealing experiments and the change of physical changes on powder and bulk system are described in Chapter 6. Finally, the summary and outlook of this project are introduced.

2 Theoretical background

The theoretical background on structural and magnetic properties of transition metal oxides are discussed in this chapter. The perovskite structure and its variants are introduced followed by an introduction into the investigated LSMO systems. Moreover, the growth methods as well as the different growth modes are discussed. Finally, a brief overview over the characterization methods for thin film systems and eventually the theory about scattering methods used in this thesis is provided.

2.1 Perovskite structure variants

Perovskite is a mineral with the formula CaTiO_3 , which was first discovered in 1839 by the Prussian mineralogist Gustav Rose and named after the Russian mineralogist Count Lev Aleksevich von Petrovski [2]. Perovskite-type oxides have the general formula ABO_3 and can be changed flexibly via not only cation and anion substitution, but also via chemical treatments. In this part, we mainly focus on the perovskite structure and the oxygen deficient brownmillerite structure.

2.1.1 Perovskite (ABO_3)

The ideal structure of perovskite is ABO_3 with the space group $\text{Pm}\bar{3}\text{m-O}_h$ [3]. Here A is usually a large cation, B usually a medium-sized cation and O^{2-} an anion. In the perovskite structure, the B cation is 6-fold coordinated and the A cation is 12-fold coordinated to the oxygen anions. **Figure 2.1(a)** shows the structure of SrTiO_3 (STO), an ideal example of the perovskite structure. From **Figure 2.1(b)** and **(c)** it can be found that the Sr^{2+} cations are located in the corners of the unit cell and the Ti^{4+} cations at the center being surrounded by a regular octahedron of oxygen anions [4].

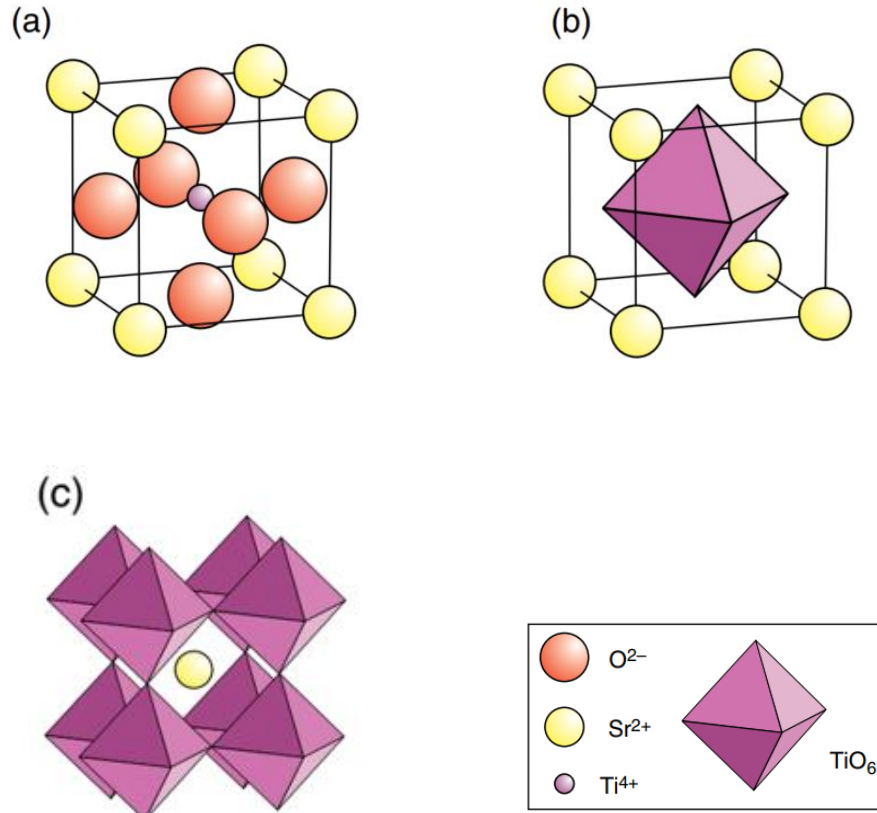


Figure 2.1 (a) Ideal SrTiO_3 crystal structure. The A and B sites are occupied by Sr and Ti respectively. (b) TiO_6 octahedral coordination polyhedron structure. (c) The relative position of a Sr atom and the TiO_6 octahedra. Figure taken from Ref [4].

2.1.2 Brownmillerite ($\text{ABO}_{2.5}$)

Brownmillerite has the chemical composition $\text{Ca}_2\text{FeAlO}_5$, which was found the first time in 1932. The brownmillerite structure can be considered as the oxygen deficient variant structure of perovskite with the formula $\text{ABO}_{2.5}$. Because this kind of structure is a member of the perovskite family, it can be directly described through the oxygen-loss process in the ideal perovskite structure as shown in **Figure 2.2(a)**. **Figure 2.2(b)** and (c) shows how this forming process occurs. The brownmillerite structure is formed by arranging rows of oxygen vacancies along the $[110]$ direction as seen in **Figure 2.2(b)**. In this configuration, each of BO_6 octahedra loses two equatorial oxygen atoms, and with a slight displacement of the B cation, the remaining four oxygen ion form a tetrahedron. Therefore, every alternative sheet of BO_6 octahedra in perovskite is transformed into a sheet containing only apex-linked BO_4 tetrahedra in the brownmillerite structure as shown in **Figure 2.2(c)** [5].

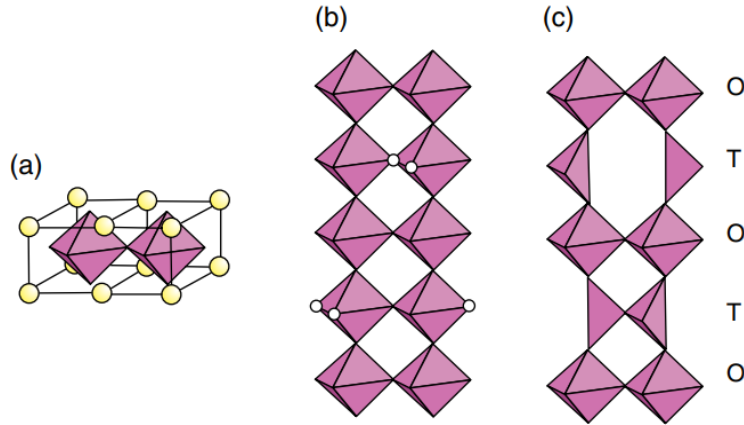


Figure 2.2 The $ABO_{2.5}$ brownmillerite Structure (a) two-unit cells from the ideal perovskite structure ABO_3 (b) The octahedral structure from an ideal perovskite structure without A cations, as well as showing the position of the deficient oxygen ions. (c) The final structure of brownmillerite, with the alternating arrangement of octahedra and tetrahedra. Fig. taken from [5].

2.2 Transition metal oxides

Metal oxides play nowadays a crucial role in many technological fields because of their variable properties. With the combination of different kinds of metal-oxygen bonds and the strong interactions between the valence electrons in the lattice [6], various transition metal oxides are studied exhibiting different functionalities [7, 8].

2.2.1 $La_xSr_{1-x}MnO_3$

In the family of transition metal oxides particularly $La_xSr_{1-x}MnO_3$ (LSMO) has been extensively studied in recent years due to its controllable properties by means of adjusting the content of the strontium cations in the perovskite structure [9, 10]. In our study, $La_{0.7}Sr_{0.3}MnO_3$ ($x=0.3$) is chosen as our system to investigate. LSMO also has a perovskite structure. **Figure 2.3** shows the structure of $La_{0.7}Sr_{0.3}MnO_3$. The A-sites are occupied by 70% lanthanum cations and 30% strontium cations.

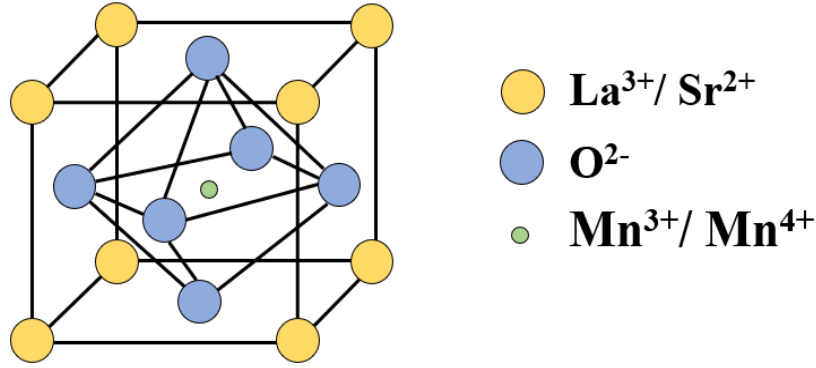


Figure 2.3 The structure of $\text{La}_{0.7}\text{Sr}_{0.3}\text{MnO}_3$. The A sites are occupied by 70% lanthanum and 30% strontium ions, the B sites are occupied by Manganese ions.

For $x=0$, i.e. LaMnO_3 , it contains Mn ions in the Mn^{3+} state. It shows an A-type antiferromagnetic ordering as shown in **Figure 2.4(a)**.

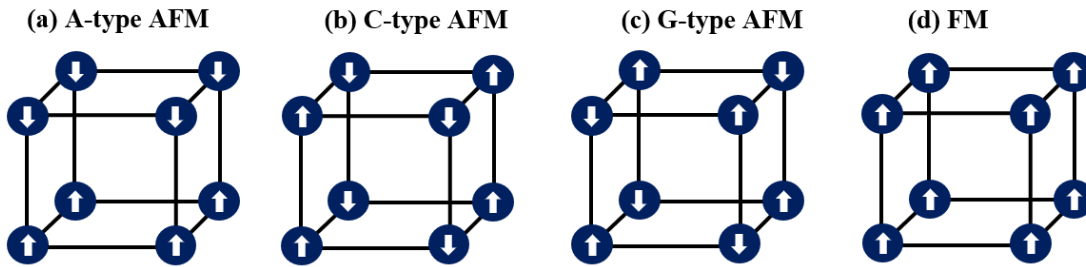


Figure 2.4 Four different types of antiferromagnetic spin order of magnetic ions which can occur on simple cubic lattices, (a) A-type AFM, (b) C-type AFM, (c) G-type AFM and (d) ferromagnetic spin order

Figure 2.5 shows the magnetic phase diagram of the $\text{La}_x\text{Sr}_{1-x}\text{MnO}_3$. When increasing the Sr content, the trivalent La^{3+} ions are replaced by the divalent Sr^{2+} . To ensure charge neutrality a fraction x of the Mn ions has to change its valency to Mn^{4+} ($t_{2g}^3 e_g^0$) while a fraction $1-x$ of the Mn ions remains as Mn^{3+} ($t_{2g}^3 e_g^1$). At $x=0.175$, the Jahn-Teller distortion effect (see next section) vanishes and the system turns to ferromagnetic behavior with a Curie temperature near 250K and being metallic [11]. In our study, the strontium content is $x=0.3$. Here the Curie temperature is 370K. In the case of a Sr content above 0.6, the system returns to antiferromagnetic behavior with C-type ordering and insulating behavior at low temperatures.

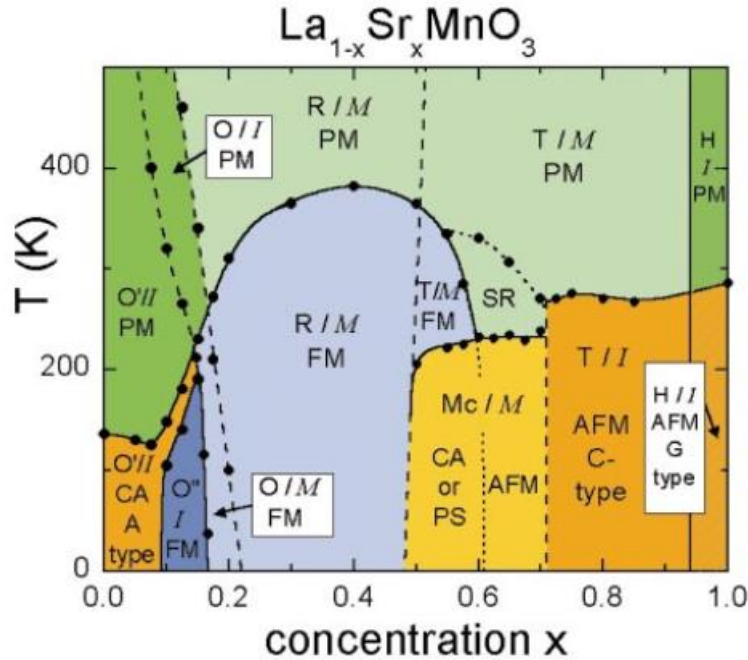


Figure 2.5 Magnetic phase diagram of $\text{La}_x\text{Sr}_{1-x}\text{MnO}_3$. Considering the structure, the symbols O, O', O'' represent orthorhombic, Jahn-Teller distorted orthorhombic and an orbital-ordered orthorhombic structure, respectively. R, T, Mc and H mean rhombohedral, tetragonal, monoclinic and hexagonal, respectively. For magnetic properties, ferromagnetic and antiferromagnetic phases are marked by FM and AFM. M and I stand for metallic and insulating behavior. Figure taken from Ref [9].

2.3 Magnetism in transition metal oxides

In transition metal oxides, the magnetic moment of the transition metal cation emerges from the d-orbital electrons. An important observation is that the magnetic moment according to theory is larger than the experimental value. This is usually due to quenching of the orbital angular moment, which is caused by the crystal field [12]. In the next section, the electronic structure and the crystal field in transition metal oxides are introduced in more detail.

2.3.1 Electronic structure

In crystal field theory, each ion is seen as a point charge, which produces an electric field to the center magnetic ion. That so-called crystal field leads to the splitting of the energy levels. When considering the crystal field, e.g. in a cubic structure, the 3d energy levels of the magnetic cation split into one threefold degenerate state t_{2g} and one twofold degenerate state e_g . The separation between e_g and t_{2g} orbitals is the so-called crystal field splitting energy Δ , which depends on the

distance between the transition metal ions and the oxygen ligands. For large Δ , it is energetically more favorable for electrons to occupy the lower set of orbitals (low spin state). Conversely, in low Δ case, it is energetically favorable for the electrons to occupy both e_g and t_{2g} orbitals according to Hund's Rules. For the manganite, the splitting energy Δ is usually in the range of 2eV [13].

As shown in **Figure 2.6**, an octahedron can distort spontaneously with decreasing the symmetry of the lattice because the energy cost of increased elastic energy is balanced by a resultant electronic energy saving due to the distortion, which is known as Jahn-Teller effect. For example, Mn^{3+} ions, which show an electron configuration of $3d^4$, show this kind of behavior. In contrast, Mn^{4+} ions ($3d^3$) would not show this kind of effect because there is no net lowering of the electronic energy by a distortion [11].

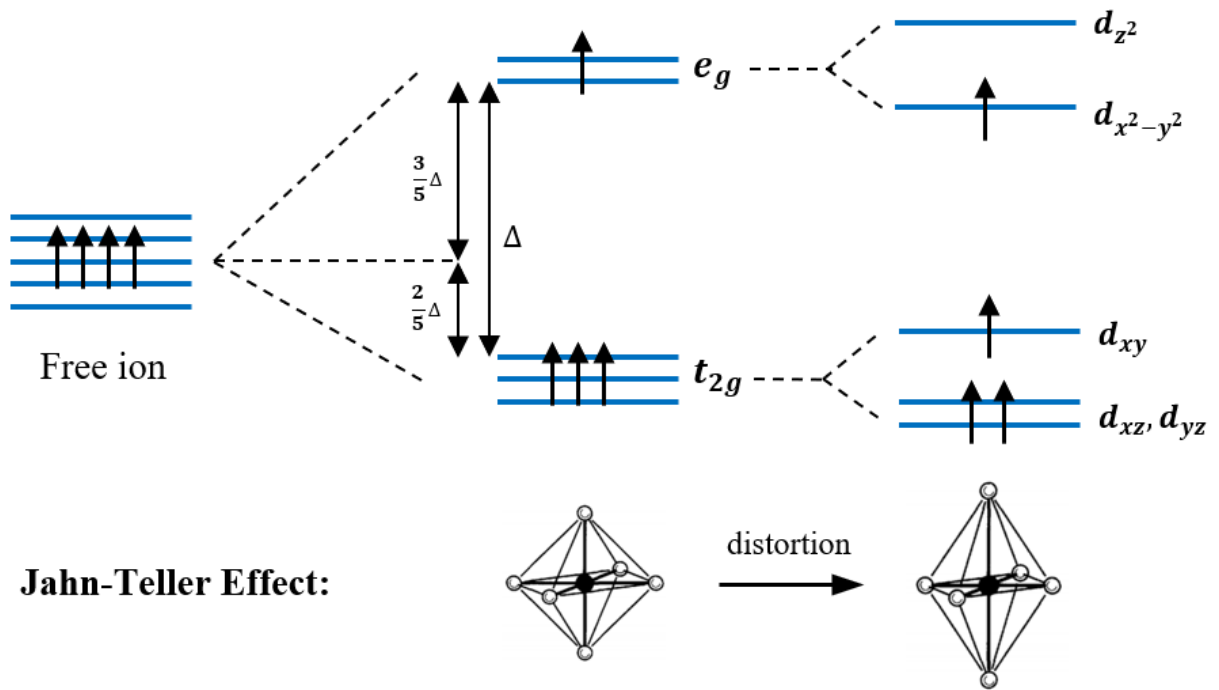


Figure 2.6 Energy levels of Mn^{3+} ($3d^4$) experiencing a crystal field and Jahn-Teller effect. An octahedral arrangement (left) can distort (right), leading to a splitting of energy levels of e_g and t_{2g} . Figure adapted from Ref [11].

2.3.2 Exchange interactions

In transition metal oxides, the magnetic and electronic transport behavior is governed by the indirect exchange interactions between the magnetic cations via the intermediate oxygen anions.

a) Super-Exchange interaction:

The magnetic order in antiferromagnetic materials, e.g. MnO and MnF₂, is usually due to the interaction between the magnetic ions via an intermediate non-magnetic ion. This type of interaction is called super-exchange interaction [14]. Assuming that, each magnetic ion would have one unpaired electron in the d orbital and each oxygen has two electrons in the p orbital as shown in **Figure 2.7**, an anti-ferromagnetic coupling is preferred by allowing these electrons to be delocalized in order to lower the energy.

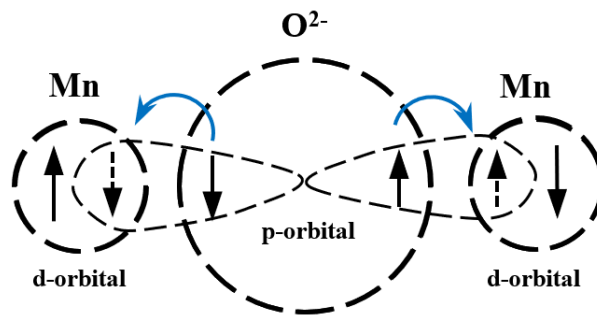
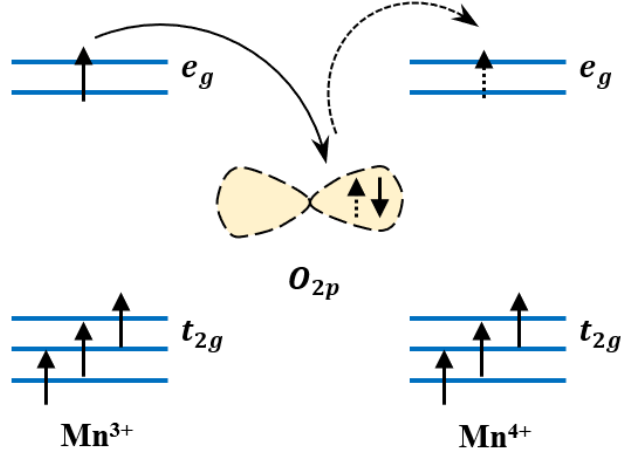


Figure 2.7 Super-exchange mechanism in MnO assuming one single unpaired electron in the d orbital of Mn and two electrons in p orbital of O. The ground state (solid arrows) and the excited state (dash arrows) of the electron spin configuration are shown if the moments are coupled antiferromagnetically. The magnetic electrons can be delocalized in this way thus lowering the energy.

b) Double-Exchange interaction

Ferromagnetic order in complex oxides is usually due to double-exchange interactions between the magnetic cations [15]. If the magnetic ions in the system have different valence, e.g. in a Mn³⁺-O-Mn⁴⁺ configuration as found in LSMO, the electrons in the e_g level of the 3d orbital of the Mn³⁺ cation have the possibility to transfer to the 2p orbital of the oxygen anion, and then transfer to the e_g level of the 3d orbital of the next Mn⁴⁺. If the spins are parallel between the Mn ions, then both the Hund's rules are satisfied at each ion and the entire system minimizes energy by delocalization of electrons between the Mn sites. Hence a parallel, i.e. ferromagnetic alignment is favored. **Figure 2.8** depicts the mechanism of double-exchange for ferromagnetic coupling.



Hopping transport

Figure 2.8 Energy levels in a Mn³⁺-O-Mn⁴⁺ configuration for ferromagnetic coupling due to double-exchange. Electron hopping can occur if the neighboring magnetic ions are ferromagnetically aligned.

2.3.3 Mean Field Theory (MFT) Approximation for a ferromagnet

Due to the exchange interaction, a ferromagnet has a spontaneous magnetization in the absence of an external magnetic field. For a ferromagnet in an applied field \vec{B} , the model Hamiltonian is:

$$\hat{H} = - \sum_{ij} J_{ij} \vec{S}_i \cdot \vec{S}_j + g\mu_B \sum_j \vec{S}_j \cdot \vec{B} \quad (2-1)$$

where J_{ij} is the exchange constant between the i^{th} and j^{th} spin. The first term describes the Heisenberg exchange energy and the second term the Zeeman energy [11].

From the Weiss model of a ferromagnet, an effective molecular field at i^{th} site can be defined as

$$\vec{B}_{mf} = - \frac{2}{g\mu_B} \sum_j J_{ij} \vec{S}_j \quad (2-2)$$

The energy consists of a Zeeman part $g\mu_B \vec{S}_i \cdot \vec{B}$ and an exchange part. The total exchange interaction between the i^{th} spin and its neighbors is $-2 \sum_j J_{ij} \vec{S}_i \cdot \vec{S}_j$. The exchange interaction is replaced by an effective molecular field \vec{B}_{mf} produced by the neighboring spins, so that the Hamiltonian becomes

$$\hat{H} = g\mu_B \sum_i \vec{S}_i \cdot (\vec{B} + \vec{B}_{mf}) \quad (2-3)$$

This is identical to the Hamiltonian for a paramagnet but in an applied magnetic field $\vec{B} + \vec{B}_{mf}$. The assumption for this approximation is that all the magnetic moments experience the same molecular field.

For a ferromagnet, the molecular field tries to align the neighboring magnetic moments, which describes the effect of the ordering of the system. Therefore, one can assume that

$$\vec{B}_{mf} = \lambda \langle \vec{M} \rangle \quad (2-4)$$

where λ parameterizes the strength of the molecular field as a function of the magnetization and $\langle \vec{M} \rangle$ is the thermodynamic approximation value of magnetization.

These ideas constitute the so-called mean field theory (MFT) [11]. **Figure 2.9(a)** shows the interactions between spins in a ferromagnetic system, the external magnetic field is depicted by \vec{B} . The assumption of MFT is illustrated in **Figure 2.9(b)**. In addition to the external field, the exchange interaction on the i^{th} spin from the neighbor spins can be considered as an internal molecular field \vec{B}_{mf} , which is proportional to the magnetization in the system.

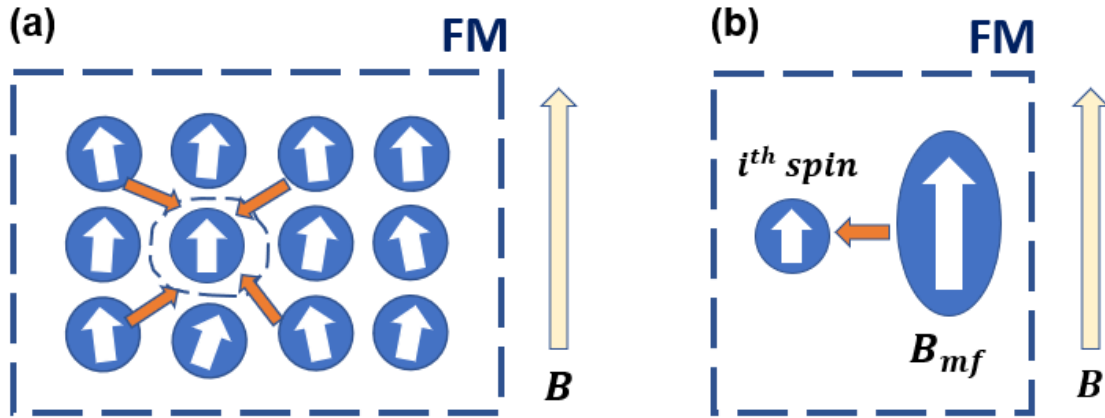


Figure 2.9 (a) The exchange interactions between spins in a ferromagnetic system with an external magnetic field \vec{B} applied. (b) The interactions between the i^{th} spin and its neighbor spins can be modeled by an internal molecular field \vec{B}_{mf} .

In our case, the orbital angular momentum L of Mn^{3+} is zero due to orbital quenching of 3d ions [16]. Thus, the exchange interaction acts between spins S .

The magnetization using the MFT can be then calculated using

$$\frac{\langle M \rangle}{M_s} = B_J(y) \quad \text{and} \quad y = \frac{g_J \mu_B J (B + \lambda \langle M \rangle)}{k_B T} \quad (2-5)$$

where M_s is the saturation magnetization, J is the total angular momentum quantum number, μ_B is the Bohr magneton and k_B the Boltzmann constant. In addition, g_J is the Landé g -value given by

$$g_J = \frac{3}{2} + \frac{S(S+1) - L(L+1)}{2J(J+1)} \quad (2-6)$$

In our case, for 3d ions, $L = 0$, thus $g_J = 2$. And $B_J(y)$ is the Brillouin function given by

$$B_J(y) = \frac{(2J+1)}{2J} \coth\left(\frac{2J+1}{2J} y\right) - \frac{1}{2J} \coth\frac{y}{2J} \quad (2-7)$$

The Curie temperature T_c , which describes the phase transition from the ferromagnetic to the paramagnetic phase, follows as [11]

$$T_c = \frac{g_J \mu_B (J+1) \lambda M_s}{3k_B} \quad (2-8)$$

2.4 Thin film growth

Thin films are widely used in a multitude of applications, e.g. in sensors, solar cells and for information technology [17-19]. Compared with bulk materials, the as-prepared state of thin films can be strongly influenced by the surface, interface, defects as well as strain effects. Therefore, it is necessary to study the growth mechanisms of thin films in order to achieve a detailed understanding of the various effects for the use in technical applications.

2.4.1 Growth methods

Thin film growth is technologically mainly performed using two approaches: Physical vapor deposition (PVD) and Chemical Vapor Deposition (CVD). As the name suggests, PVD is the method without chemical reactions during the thin film growth process. Examples of this approach

are: thermal evaporation, Molecular Beam Epitaxy (MBE), sputtering and Pulsed Laser Deposition (PLD). In this study, the sputtering method is used to grow the thin film samples.

2.4.2 Growth modes

During the thin film growth process, deposited atoms (or molecules) are adsorbed by the substrate followed by a diffusion process on the surface. Three different growth modes can be distinguished as shown in **Figure 2.10** [20, 21].

- a) **Frank-van-der-Merve mode:** When the relationship between surface energy of the film γ_{film} , interface energy between film and substrate $\gamma_{interface}$ and the surface energy of the substrate $\gamma_{substrate}$ meets the condition $\gamma_{film} + \gamma_{interface} \leq \gamma_{substrate}$, then layer by layer growth is obtained which results in a smooth film.
- b) **Volmer-Weber mode:** When the relationship meets the condition: $\gamma_{film} + \gamma_{interface} \geq \gamma_{substrate}$, an island growth mode is preferred.
- c) **Stranski-Krastanov mode:** In this case first a monolayer is formed and subsequently island growth dominates. This occurs in the case of: $\gamma_{film} + \gamma_{interface} + \gamma_{misfit} \geq \gamma_{substrate}$. Usually, this mode is due to large lattice misfits in epitaxial growth. When forming the first layer, the misfit energy is not large enough and hence the first layer grows epitaxially. With increasing layer thickness strain energy builds up until island growth dominates due to lowering of strain energy.

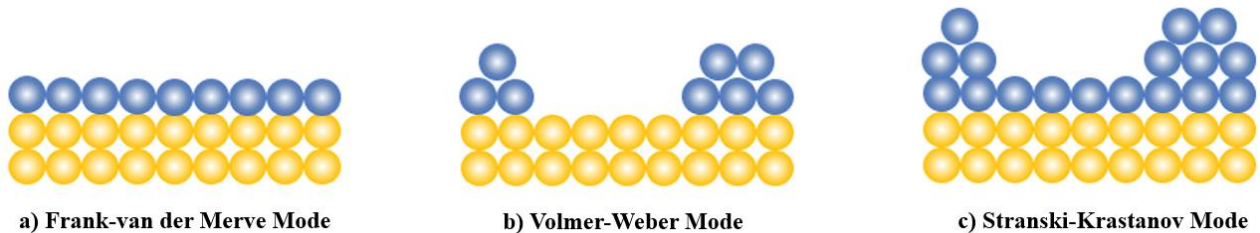


Figure 2.10 Three different modes of thin film growth. a) Frank-van der Merve mode: layer by layer growth b) Volmer-Weber mode: island growth c) Stranski-Krastanov mode: first layer by layer growth then island growth.

2.5 Scattering theory

Crystals can be considered as 3D periodic arrays of atoms. In order to investigate the microscopic structure of crystals non-destructively, scattering methods are used to collect the structural information of the material. In this thesis, a brief introduction to X-Ray diffractometry and reflectometry as well as polarized neutron reflectometry is given. **Figure 2.11** introduces the basic scattering experiment in Fraunhofer approximation, where the size of the sample is much smaller than the distance between the sample and source as well as between sample and detector.

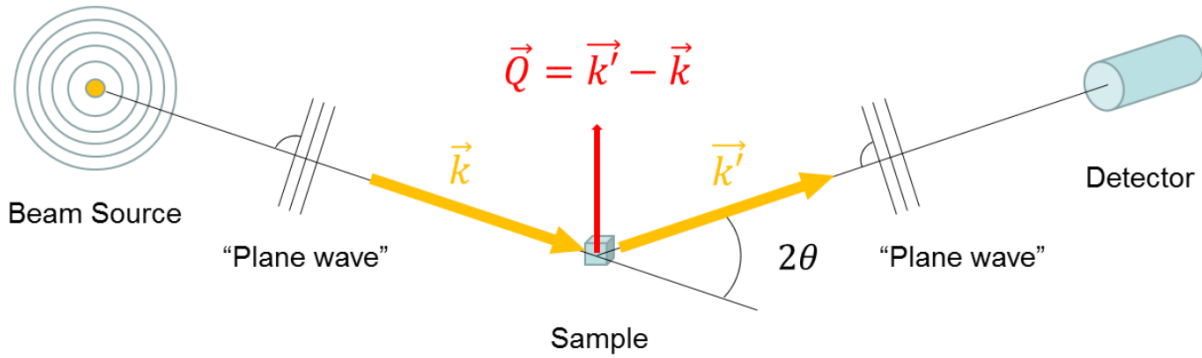


Figure 2.11 Sketch of the basic scattering process with the incoming wave characterized by wave vector \vec{k} , diffracted wave by \vec{k}' and the scattering vector \vec{Q} . Assumed is: plane waves for incident beam, source-sample and sample-detector distances are much larger than the sample size [22]. Fig. taken from Ref [23].

In the case of elastic X-ray scattering, the incident and diffracted wave vectors have a relationship as

$$|\vec{k}| = |\vec{k}'| = \frac{2\pi}{\lambda} \quad (2 - 9)$$

Then so-called scattering vector \vec{Q} is defined as

$$\vec{Q} = \vec{k}' - \vec{k} \quad (2 - 10)$$

The magnitude of the scattering vector can be calculated from the wavelength λ and scattering angle 2θ as follows

$$Q = |\vec{Q}| = \sqrt{\vec{k}^2 + \vec{k}'^2 - 2\vec{k}\vec{k}' \cos 2\theta} \rightarrow Q = \frac{4\pi}{\lambda} \sin \theta \quad (2 - 11)$$

2.5.1 X-Ray diffractometry (XRD)

X-rays are an ideal probe to characterize crystal structures due to the similar length scales, i.e., of the wavelengths of X-rays and the atomic lattice spacings. **Figure 2.12** shows an X-ray diffractometry experiment. When the incident beam interacts with the lattice, constructive interference patterns occur when Bragg's law (Equation 2-12) is satisfied [24]. Here d is the lattice parameter, λ is the wavelength of the incident beam, θ is the incident angle.

$$2d\sin\theta = n\lambda \quad (2 - 12)$$

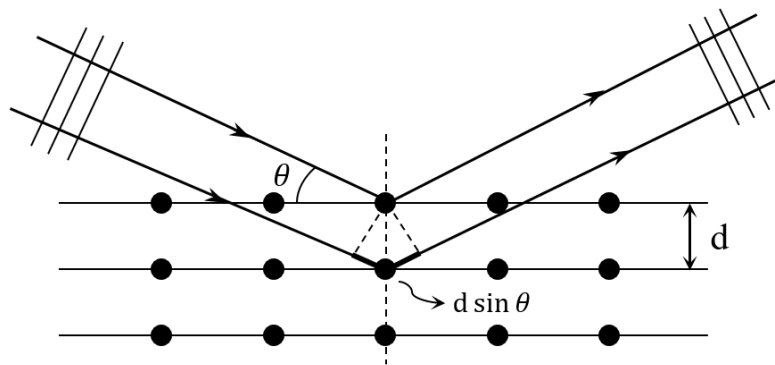


Figure 2.12 Sketch of an X-ray diffractometry experiment, showing Bragg's Law.

2.5.2 X-Ray reflectometry (XRR)

X-ray reflectometry is surface sensitive characterization method widely used for the study of surfaces, interfaces in thin films and multi-layer systems [25]. The typical sketch of an XRR measurement is shown in **Figure 2.13**, the incident beam is reflected from the surface.

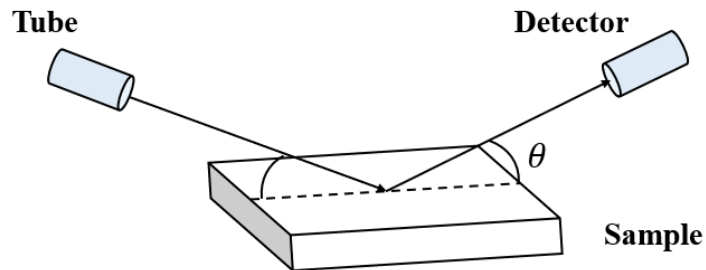


Figure 2.13 Sketch of an X-ray reflectometry experiment.

For most materials, the index of refraction n for X-rays is smaller than 1, leading to a total reflection for small incident angles below the so-called critical angle θ_c [25], which is defined as:

$$\theta_c = \arccos n \quad \theta_c \cong \lambda \sqrt{\frac{\rho}{\pi}} \quad (2 - 13)$$

where λ and ρ represent the wavelength as well as the electron density for X-rays.

For large incident angle above θ_c , the beam can partially penetrate the sample and is only partly reflected with a decrease by Q^{-4} for a flat surface [26].

For a single thin film system with thickness d , constructive interference occurs between beams reflected from the surface of the thin film and the reflected beam from the interface between the layer and substrate, which is called ‘‘Kiessig fringes’’ [22]. An oscillation pattern due to the above-described interference effect can be observed with a period:

$$\Delta Q = \frac{2\pi}{d} \quad (2 - 14)$$

The film thickness can be determined accordingly with $d = \frac{2\pi}{\Delta Q}$.

The reflectivity is highly sensitive to the roughness of the surface and the interface. In a real system, the thin film always shows a certain roughness in the order of nanometers, which leads to a diffuse scattering of the incident beam. A strong decay of the reflectivity and damping of the oscillation with increasing Q can be observed for a rough surface or interfaces. Therefore, the XRR method is also used to determine the roughness of the surface and the interfaces.

2.5.3 Reciprocal space mapping (RSM)

Reciprocal space mapping is very useful to determine the strain status of epitaxial thin film layers. Assuming that the vector of a cubic crystal is $(\vec{a}_1, \vec{a}_2, \vec{a}_3)$, then the reciprocal vectors are defined as follows:

$$\vec{b}_1 = 2\pi \frac{\vec{a}_2 \times \vec{a}_3}{\vec{a}_1 \cdot (\vec{a}_2 \times \vec{a}_3)} \quad \vec{b}_2 = 2\pi \frac{\vec{a}_3 \times \vec{a}_1}{\vec{a}_2 \cdot (\vec{a}_3 \times \vec{a}_1)} \quad \vec{b}_3 = 2\pi \frac{\vec{a}_1 \times \vec{a}_2}{\vec{a}_3 \cdot (\vec{a}_1 \times \vec{a}_2)} \quad (2 - 15)$$

The lattice constant is then $\frac{2\pi}{a}$. Therefore, the reciprocal lattice vector \vec{K}_{hkl} around the (hkl) reflection can be written as:

$$\vec{K}_{hkl} = h\vec{b}_1 + k\vec{b}_2 + l\vec{b}_3 \quad (2 - 16)$$

which stands perpendicular to the (hkl) planes, with the relationship to the lattice parameter of a biaxially strained cubic crystal (hkl) planes d_{hkl} :

$$|\vec{K}_{hkl}| = \frac{2\pi}{d_{hkl}} \quad (2 - 17)$$

$$|\vec{K}_{hkl}|^2 = \frac{4\pi^2}{d_{hkl}^2} = 4\pi^2 \left(\frac{h^2 + k^2}{a_x^2} + \frac{l^2}{a_z^2} \right) = K_x^2 + K_z^2 \quad (2 - 18)$$

The scattering vector K_x and K_z depends on the lattice parameter a_x and a_z respectively, thus, the lattice constants a_x and a_z can be derived as follows:

$$K_x^2 = 4\pi^2 \left(\frac{h^2 + k^2}{a_x^2} \right) \rightarrow a_x = \frac{2\pi}{K_x} \sqrt{h^2 + k^2} \quad (2 - 19)$$

$$K_z^2 = 4\pi^2 \left(\frac{l^2}{a_z^2} \right) \rightarrow a_z = \frac{2\pi}{K_z} l \quad (2 - 20)$$

Figure 2.14 shows the geometry of an RSM measurement in reciprocal space with incoming and outgoing beam with vector \vec{k} and \vec{k}' . The scattering vector \vec{Q} is decomposed into the \vec{Q}_x and \vec{Q}_z component:

$$\vec{Q}_x = \vec{Q} \sin(\omega - \theta) = \frac{4\pi}{\lambda} \sin \theta \sin(\omega - \theta) \quad (2 - 21)$$

$$\vec{Q}_z = \vec{Q} \cos(\omega - \theta) = \frac{4\pi}{\lambda} \sin \theta \cos(\omega - \theta) \quad (2 - 22)$$

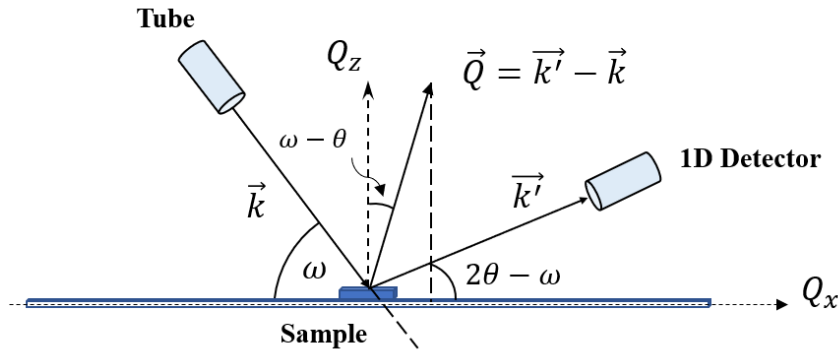


Figure 2.14 Geometry of incoming and outgoing beam during an RSM measurement.

Figure 2.15 shows the two different strain states of a thin film grown on a substrate with different lattice parameter. The fully strained and fully relaxed lattice structures as well as their reciprocal space mapping are shown in **Figure 2.15(a)** and **(b)** [27]. For the fully strained case, the in-plane lattice constant of the thin film a_{\parallel} is the same as the lattice parameter of the substrate a_s . In the reciprocal space mapping, the same Q_x can be observed. While the out of plane lattice parameter a_{\perp} is not strained by the substrate, thus showing its own lattice parameter. For the fully relaxed case, when the thickness of the film exceeds some critical value during deposition, the in-plane lattice parameter is no longer the same as the substrate, thus $a_{\parallel} \neq a_s$. As a consequence, if the eigen lattice constant of the film is larger than the substrate, the Q_x in the reciprocal space mapping moves to lower value while the Q_z shifts to larger value due to the Poisson's ratio.

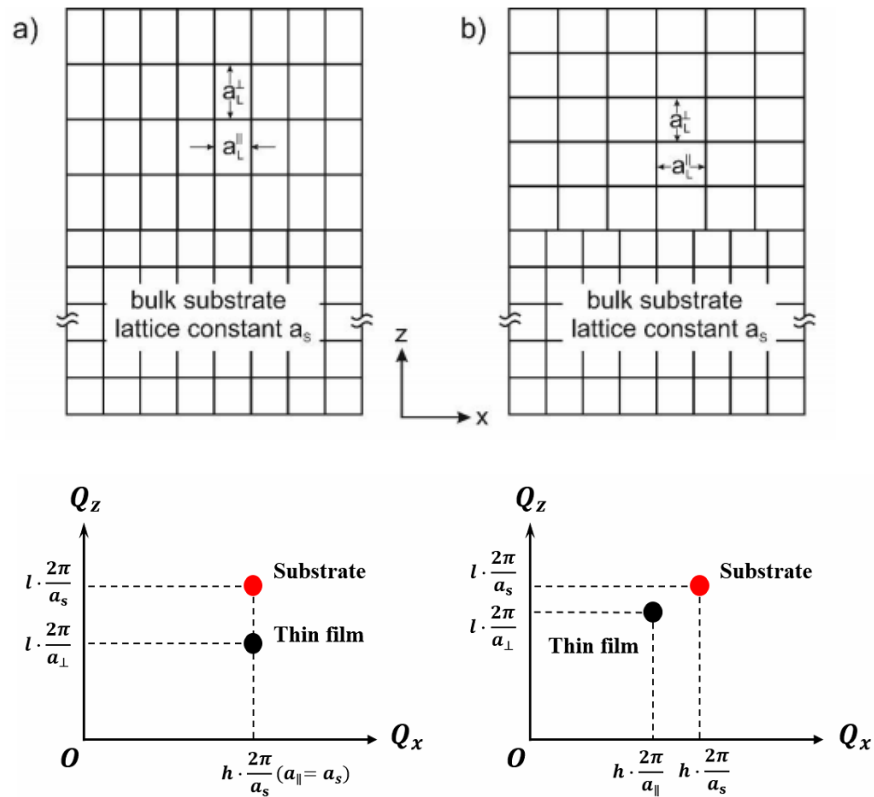


Figure 2.15 The crystal lattice structures of epitaxial thin films in the real space and their reciprocal space mapping for (a) fully strained (b) fully relaxed cases. Figure adapted from [27].

2.5.4 Polarized neutron reflectometry (PNR)

Neutrons and X-rays interact with a material differently. X-rays primarily interact with the electron cloud, which leads to a larger contribution to the diffracted X-ray intensity for atoms with a larger

atomic number (Z). On the other hand, neutrons interact with the nucleus, which results in different contributions between different isotopes, e.g., hydrogen and deuterium. In addition, neutrons have no electrical charge and hence can penetrate matter to large depths. However, they carry a magnetic moment and therefore can interact with the internal magnetic field created by magnetic moments, which provides the possibility to investigate the microscopic magnetic structure.

Compared to X-ray reflectometry, Polarized Neutron Reflectometry has several advantages. Most notably, neutron scattering methods are more sensitive for measuring light elements, e.g. hydrogen, oxygen, nitrogen and carbon, because neutrons probe the nuclear contrast rather than the electron density.

Due to Zeeman interactions between the magnetic moment of neutrons and magnetic induction of the sample, the interaction potential for neutrons can be described as [22]:

$$V(\vec{r}) = \frac{2\pi\hbar^2}{m_N} \rho_N b - \gamma_N \mu_N \vec{\sigma} \cdot \vec{B} \quad (2 - 23)$$

The first term describes the nuclear potential, and the second term corresponds to the magnetic contribution of the scattering potential with the gyromagnetic factor for neutrons ($\gamma_N = -1.913$), where ρ_N is the nuclear number density and b is the scattering length; μ_N is the nuclear magneton, $\vec{\sigma} = \{\hat{\sigma}_x, \hat{\sigma}_y, \hat{\sigma}_z\}$ is the spin operator which consists of Pauli-matrices and \vec{B} denotes the magnetic induction field.

The general geometry of PNR as measured on the instrument MARIA (MLZ) is shown in **Figure 2.16(a)**. The sample is installed vertically, and a saturating magnetic field is applied on the sample to align the spins in one direction. In the PNR measurement, the neutron beam is polarized parallel and anti-parallel to the applied magnetic field and the polarized neutron beam with two spin components $\psi_+(\vec{r})$ and $\psi_-(\vec{r})$ can be described as “spin-up” and “spin-down” polarization with respect to the quantization axis. The three-dimensional Schrödinger equation can be expressed with the neutron wave function:

$$\psi_+''(\vec{z}) + \left[k_z^2 - 4\pi b \rho_N + \frac{2m\gamma_N \mu_N}{\hbar^2} B_{\parallel} \right] \psi_+(z) + \frac{2m\gamma_N \mu_N}{\hbar^2} B_{\perp} \psi_-(z) = 0 \quad (2 - 24)$$

$$\psi_-''(\vec{z}) + \left[k_z^2 - 4\pi b \rho_N + \frac{2m\gamma_N \mu_N}{\hbar^2} B_{\parallel} \right] \psi_-(z) + \frac{2m\gamma_N \mu_N}{\hbar^2} B_{\perp} \psi_+(z) = 0 \quad (2 - 25)$$

where B_{\parallel} and B_{\perp} are the magnetic field of the sample parallel and perpendicular to the neutron guide field. For the component B_{\parallel} , the differential equations are decoupled, leading to nuclear and magnetic scattered intensities observed only in the so-called non-spin-flip channel. In more detail, the spin up (R++) channel shows the sum of the nuclear and magnetization contribution, while the spin down-down (R--) channel shows the difference. If the perpendicular component $B_{\perp} \neq 0$, the equations above are not decoupled, thus slip-flip event occurs, which will not be discussed further.

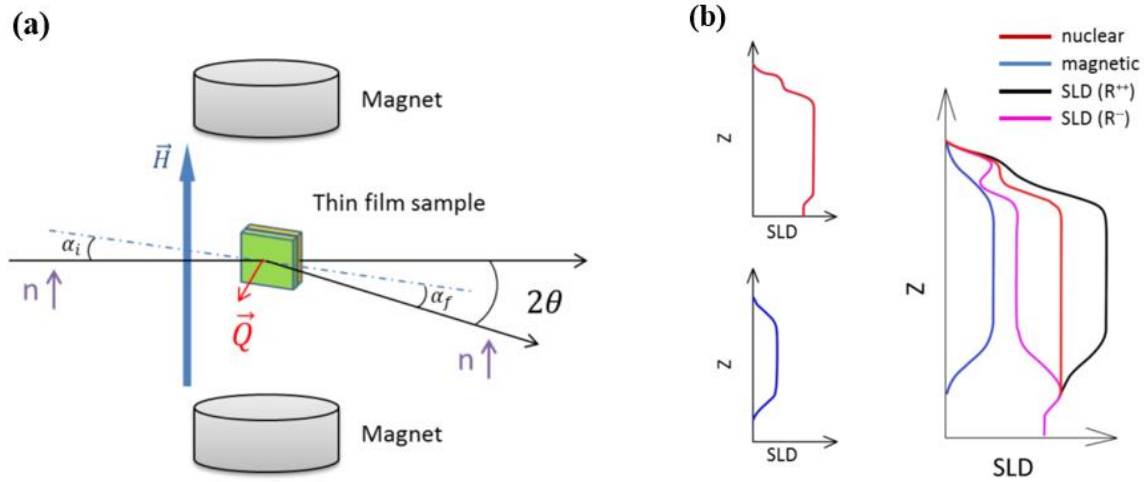


Figure 2.16 (a) Scattering geometry of a polarized neutron reflectivity experiment (b) Plot of the scattering length densities as function of film depth [23]. Figure taken Ref [23].

Neutron beam reflectometry is employed at very small wavevectors, usually $Q_{\perp} < 0.3 \text{ \AA}^{-1}$ [28]. In this range, the scattering medium consists of a continuous number density of N each with coherent neutron scattering length b . Thus, the nuclear scattering length density (NSLD) is defined as

$$\rho_n = \sum_i^J N_i b_i \quad (2-26)$$

where J is the number of distinct isotopes, N_i and b_i are the number density and scattering length for the i^{th} species.

At saturation field, all the spins are aligned to the direction of external magnetic field. The neutron magnetic scattering length density (MSLD) is

$$\rho_m = \sum_i^J N_i p_i = C \sum_i^J N_i \mu_i \quad (2 - 27)$$

where N_i is the number density; p_i and μ_i are the magnetic scattering length and magnetic moment, respectively; C is constant = $2.645 \times 10^{-5} \text{Å} \cdot \mu_B^{-1}$.

Because the nuclear and magnetic Scattering Length Densities (SLD) are of the same order of magnitude, PNR is in particular sensitive to magnetic structures. **Figure 2.16(b)** shows the typical SLD of the spin-up and spin-down signal in a semi-polarized experiment, together with the sum and the difference of the spin-up and spin-down contribution and the nuclear and magnetic SLD as a function of depth.

3 Experimental methods and instruments

In this chapter, the instruments which are used for the preparation and characterization of the sample are briefly introduced. For sample preparation the High Oxygen Pressure Sputtering Deposition (HOPSD) method is used. X-ray reflectometry can provide information on the structure and surface of thin film samples. In order to investigate the magnetic and electric properties a SQUID magnetometer (MPMS XL) and a PPMS device from the company Quantum Design are used. Moreover, the XAS and XMCD measurements are performed to investigate the valence states of magnetic ions and its magnetization at the BESSY synchrotron. In addition, PNR measurements on MARIA at MLZ are employed to study the magnetic depth profile of the as-prepared thin film samples.

3.1 High Oxygen Pressure Sputtering Deposition (HOPSD)

Epitaxial thin films of $\text{La}_{0.7}\text{Sr}_{0.3}\text{MnO}_3$ are grown on SrTiO_3 substrates by HOPSD. **Figure 3.1** shows the schematic of the sputtering machine. Sputter deposition is a type of PVD process and the entire sputtering process can be divided into three steps:

- Oxygen plasma creation by applying a high voltage on the target
- Target atoms ejection by bombardment of ionized atoms
- Deposition of target material onto the substrate

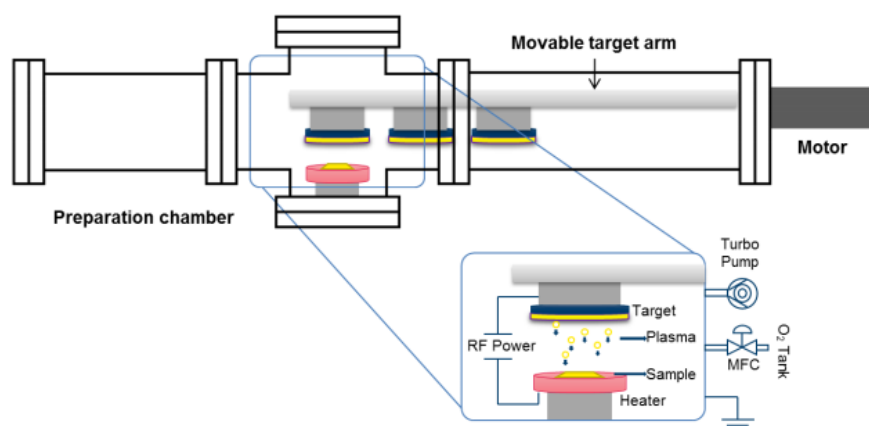


Figure 3.1 Schematics of the sputter deposition system [29]. The target diameter is 5cm, the distance between the target and the substrate is usually 2cm. Figure adapted from [29].

Compared to a common sputtering machine, which usually operates under high vacuum in the range of 10^{-3} to 10^{-6} mbar, the deposition process for HOPSD is at high oxygen pressures of 1-3 mbar, resulting in a short mean free path of the sputtered material as well as the localization of the plasma, suppressing the back-sputtering effects of the deposited layer [30]. This effect highly depends on the pressure and the distance between target to sample. The optimal distance is 2cm in our case.

Before the sputtering process, it is essential to evacuate the chamber to 10^{-6} mbar in order to achieve an acceptable base pressure. Then “Pre-sputtering” is used to clean the target from contaminants. It is necessary to leave the substrates during this process in their starting position as far away as possible from the targets, so that no unwanted coating can occur. Then for film deposition the target is positioned above the substrate. While growing the film, the stage is heated to 800 °C and the oxygen pressures are in the range of 0.5 mbar to 3 mbar, which can be controlled via a mass flow controller.

3.2 X-Ray Reflectometry/ Diffractometry (XRR and XRD)

The X-ray reflectometer “D8 Advanced” from Bruker AXS is used to characterize the thin film samples. A schematic is shown in **Figure 3.2**. At low angles (X-ray reflectivity (XRR) mode) in particular the surface is probed. At high angles the crystallographic structural information can be obtained. The X-ray source is a Cu-source with a wavelength of $\lambda = 1.54 \text{ \AA}$. Additionally, a heating stage as well as a vacuum chamber are installed to provide an in-situ annealing environment. At these conditions, the sample can be annealed up to 750 °C at high vacuum (base pressure 10^{-6} mbar).

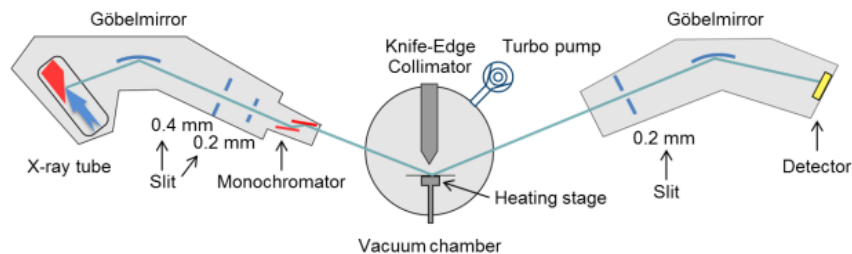


Figure 3.2 Sketch of the Bruker D8 X-Ray Reflectometer with the installed vacuum chamber and heating stage. Figure taken from Ref [31].

In this study, the reciprocal space mapping is performed on a Bruker D8 at PGI-7 by Dr. Felix Gunkel and Moritz Weber.

In addition, LSMO powder samples are characterized on a powder diffractometer in transmission geometry with a Huber Imaging Plate Guinier Camera G670 equipped with Cu $K\alpha$ - or Mo $K\alpha$ -radiation. The accessible temperature range reaches from 10 to 300 K using a closed-cycle cryostat and from 673 to 1773 K using a laser heating module.

3.3 SQUID magnetometry (MPMS)

The macroscopic magnetic properties of the thin film samples are investigated by a Superconducting Quantum interference Device (SQUID) magnetometer (model MPMS XL from Quantum Design). **Figure 3.3** shows the basic principle of the MPMS SQUID magnetometer. A vertical magnetic field from -7T to 7T can be applied to the sample using a superconducting solenoid.

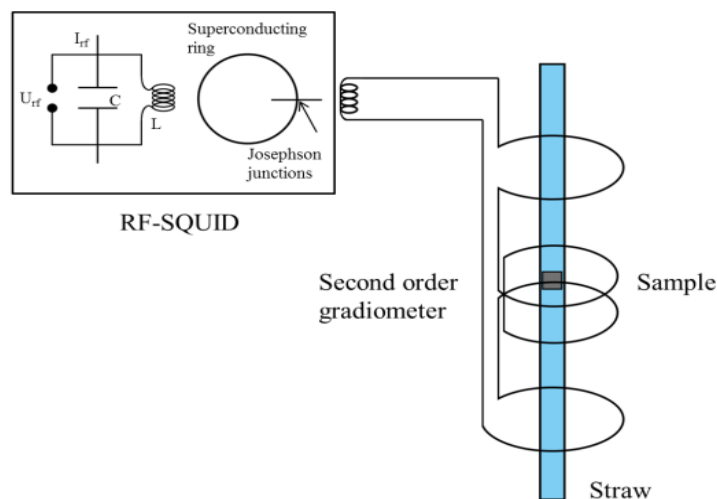


Figure 3.3 Sketch of the detection system of the MPMS SQUID magnetometer. The sample is mounted on a straw. Figure taken from [23].

The sample is mounted on a straw and is moved up and down through the pick-up coils, which is a second order gradiometer coil. A current is thus induced in the gradiometer coil. This gradiometer is coupled to a RF-SQUID circuit, which consists of a superconducting ring with a Josephson junction as well as a LC circuit. An additional magnetic flux is produced by the current transferred

from the pick-up coil to the SQUID ring. From the response of the SQUID ring inside the LC circuit the original induced current in the pick-up coil is detected with high accuracy. The resolution of the SQUID magnetometer is in the order of $10^{-10} \text{ A}\cdot\text{m}^2$.

Two measurement modes, direct current mode (DC) and reciprocating sample option mode (RSO) can be used on the SQUID magnetometer. In the DC mode, the sample moves through the pickup coil in discrete steps, while during the RSO mode the sample oscillates harmonically around the measurement position, which provides a faster measurement and better noise rejection than the DC mode.

3.4 Physical Properties Measurement System (PPMS)

The electronic transport properties of the thin film samples are studied using a Physical Property Measurement System (PPMS) from Quantum Design.

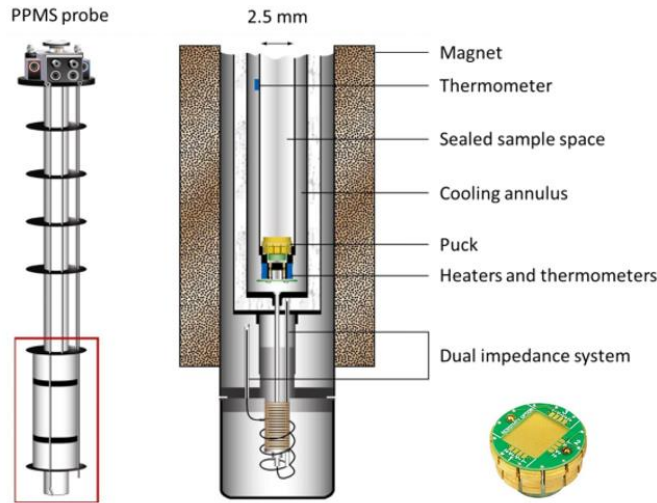


Figure 3.4 Sketch of the resistivity measurement mode of the PPMS system with a so-called resistivity puck. The sample is glued onto the golden plateau on the puck and contacted using thin platinum wires. Figure taken from Ref [32].

The resistivity from 5K to 400K is measured at magnetic fields of 0T, 5T, 9T, respectively. Moreover, the magnetoresistance of the samples with different growth parameters is also investigated. **Figure 3.4** shows the sketch of the “resistivity mode” of the PPMS device. For resistivity measurements of thin film samples the Van-der-Pauw method is used [33]. In our case, platinum wires are connected to the four edges of the thin film surface using silver paint. For the

Van-der-Pauw method, the 2D sample must be homogenous and isotropic with a flat shape and uniform thickness. In addition, all four contacts should be located at the edge of the sample and must be much smaller than the sample size. An average qualitative resistivity value of the thin film sample can then be obtained.

For bulk samples, the 4-wire method is used to measure the electronic transport property.

3.5 Polarized Neutron Reflectometry (PNR)

In order to investigate the magnetic depth profile of the thin films, PNR was employed on the instrument MARIA at MLZ. **Figure 3.5** and **Figure 3.6** show the basic configuration of MARIA.

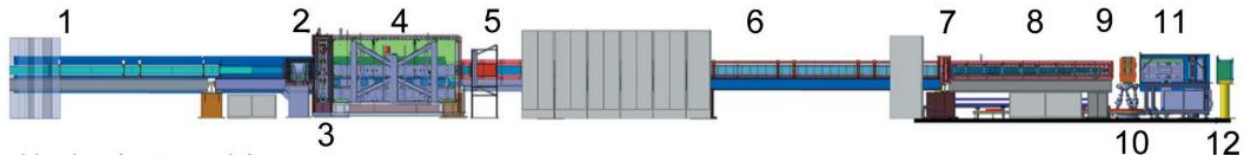


Figure 3.5 Side view of MARIA, starting on the left with (1) casemate wall, (2) velocity selector, (3) lift with neutron guide and two Fermi chopper positions, (4) polarization chamber and lift with three positions, (5) radio frequency (RF) flipper, (6) elliptical vertically focusing NG (from 4 to 9), (7) slit S1, (8) collimation base, (9) slit S2, monitor 1 and attenuators, (10) hexapod with sample position and optional magnet, (11) detector arm with ^3He filter and ^3He two-dimensional position sensitive detector, and (12) beam stop. Figure taken from Ref [34].

MARIA is optimal for thin film samples with thickness between 3\AA and 300\AA and lateral structure sizes from nm to μm sizes. The wavelength of the incoming neutrons is selected by a velocity selector in the range of $4.5\text{\AA} < \lambda < 40\text{\AA}$, with a maximum intensity at $\lambda = 4.5\text{\AA}$. The resulting wavelength resolution is $\Delta\lambda/\lambda = 10\%$. On MARIA the neutron beam can also be polarized by a polarizing guide and analyzed by a wide angle ^3He -cell. Different scattering channels (e.g., non-spin-flip and spin-flip) can be distinguished to reveal the orientation of the magnetization. The sample is mounted on a holder at a 10^{-6} mbar vacuum with an available temperature range from 5K to room temperature. For analyzing the neutron data, the software GenX is used to quantify the structural and magnetic depth profile.

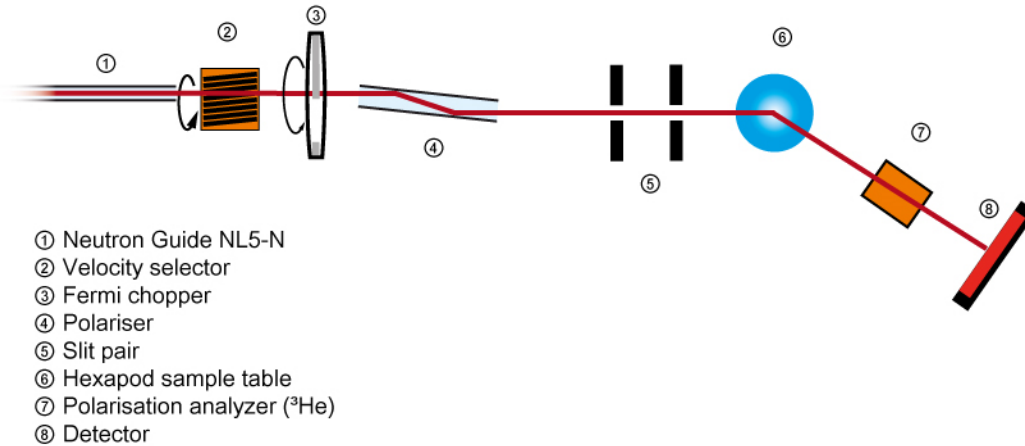


Figure 3.6 Sketch of selected parts of the MARIA instrument. The polarized neutron beam is focused onto the sample surface by passing the velocity selector, polarizer and slit pair. Figure taken from [35].

3.6 Rutherford Backscattering Spectrometry (RBS)

Rutherford Backscattering spectrometry (RBS) is a near-surface sensitive method to determine the structure and the depth profile of the concentration of elements based on the elastic collisions between the He^{2+} particles with high kinetic energy from the incident beam and the particles located in the sample. RBS measurement is in particular sensitive to heavy atoms and less for light elements.

The RBS measurements in this study are carried out by Dr. Lei Cao at Helmholtz Zentrum Dresden Rossendorf (HZDR) in Dresden. **Figure 3.7** shows the basic sketch of an RBS measurement. A beam of high energy ions (typically protons or alpha particles) is accelerated to 1.6MeV with typically a beam current of 10-20nA. It then impinges on the sample and the energy loss of backscattered particles according to the Rutherford backscattering effect are measured by an energy sensitive detector at an angle of 170° . From this the depth profile of different atom species can be obtained.

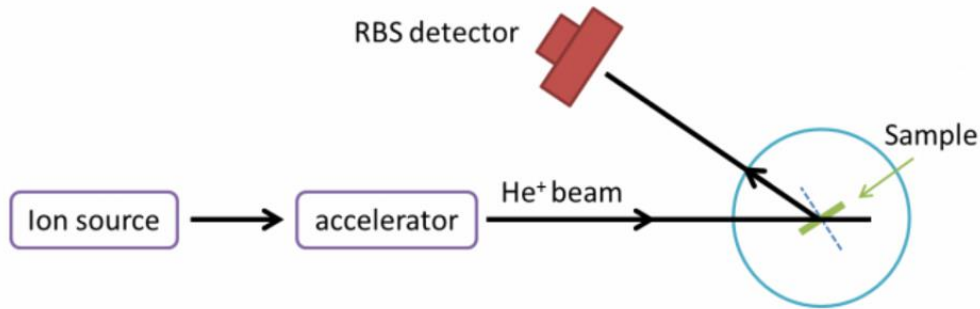


Figure 3.7 Sketch of an RBS measurement. A He ion beam is accelerated towards the sample and then backscattered at some certain angle. The energy loss of the He particles can be detected by an energy sensitive detector. Figure taken from [23].

3.7 X-ray Absorption Spectroscopy and X-Ray Magnetic Circular Dichroism (XAS and XMCD)

X-ray absorption spectroscopy (XAS) is widely used to investigate the electronic structure of system. In order to obtain intense and tunable X-ray beams, the experiments are usually performed at synchrotron radiation facilities. In this study, the XAS and XMCD measurements are employed by Dr. Tomas Duchon at BESSY in Berlin.

Figure 3.8 shows the basic concept of an XAS measurement. The inner shell electrons can be ionized when the energy of the external radiation is larger than their binding energy. Because the absorption spectrum is strongly related to the electronic configuration of the atoms and the energy band structure, the composition and the valence states of the elements can be measured. According to the main shell states of the elements (K shell, L shell, etc.), the X-ray absorption spectrum shows absorption features named as K, L edge and so on.

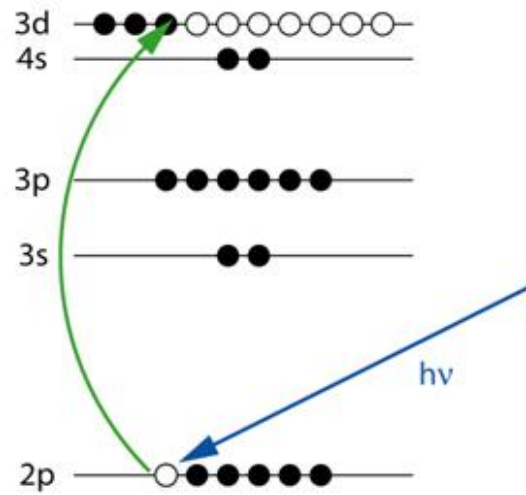


Figure 3.8 Sketch of the basic process in an XAS measurement. The electrons from an inner shell can be activated to higher states and thus the absorption energy, which is sensitive to the chemical composition and the band structure, can be probed. Figure taken from [36].

X-Ray magnetic circular dichroism spectroscopy (XMCD) is a variant of XAS which can measure the spin and orbital magnetization by circularly polarized X-ray radiation.

4 Structural and physical properties of as-prepared LSMO thin films

This chapter describes the substrate pre-treatment and growth parameter study of $\text{La}_{0.7}\text{Sr}_{0.3}\text{MnO}_3$ (LSMO) thin films, which are prepared by High Oxygen Pressure Sputter Deposition (HOPSD). The phase transition process is strongly influenced by the as-prepared state of samples, the structural and physical properties of the thin films are firstly investigated.

4.1 Sample preparation

4.1.1 Substrate Selection

The substrate is usually considered as one of the main parameters for thin film sample growth. Due to the lattice mismatch between the substrate and thin film either tensile or compressive strain can be applied to the thin film. A lattice mismatch of less than 7% - 9% is usually required for epitaxial film growth [37].

In **Figure 4.1** the lattice expansion induced by increasing temperature in different materials is shown. At around 105K the anti-ferro distortive structural phase transition of STO occurs with rotation of adjacent TiO_6 octahedral and lowering of the symmetry from cubic to tetragonal [38]. Moreover, the lattice parameter change is relatively small with decreasing temperature. Thus, single-crystalline STO substrates are ideal for the annealing experiments as shown below. In our study, single-side polished STO substrates in (001) orientation from the companies CRYSTEC or SHINKOSHA are used due to its simple chemical composition and stable structure. On the other hand, the lattice parameters of bulk LSMO and bulk STO at room temperature are 3.88\AA and 3.90\AA , respectively [39]. Therefore, the lattice small lattice mismatch between LSMO and STO is very small (around 0.6%).

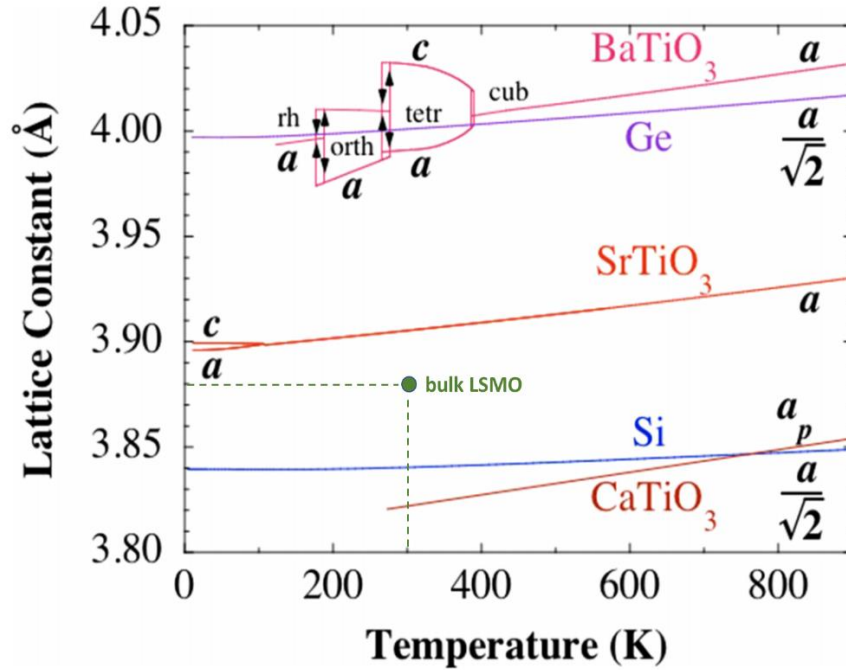


Figure 4.1 Phase transitions and lattice parameter changes for various substrate materials as function of temperature [40]. Figure taken from Ref [40].

4.1.2 Growth parameters

$\text{La}_{0.7}\text{Sr}_{0.3}\text{MnO}_3$ thin films are prepared by HOPSD. The LSMO target (Size: 12.0'' diameter \times 0.125'' thickness) is purchased from Kurt J. Lasker Company with a purity of 99.9%. After the substrate is placed inside the sputter system, the chamber is pumped by a backing pump and a turbo pump to reach high vacuum conditions of ca. 10^{-6} mbar. For achieving high-quality film growth, it is necessary to first clean the surface of the STO substrate by heating it to 950°C for 2 hours, which not only removes the adatoms and molecules, but also provides atomically smooth surfaces of STO substrates [41].

During the deposition process, five parameters should be taken into consideration: plasma power, growth temperature, the distance between the sample holder and the target, oxygen pressure and the growth time. The distance, plasma power and growth temperature mainly influence the kinetic process of growth, e.g. nucleation and diffusion of adatoms. The oxygen pressure tunes the amount of oxygen vacancies in the lattice, while the growth time determines the thickness of the thin films. In the previous work, it was found that 120W plasma power is the optimal for LSMO thin film

deposition and the optimal oxygen pressure, growth temperature and growth distance are 2mbar, 800°C and 2cm, respectively [23].

Table 4.1 shows the investigated growth parameters used in this study.

Table 4.1 Growth parameters used in this study for LSMO thin films.

Sample ID	Size [mm×mm]	Temperature [°C]	Oxygen pressure [mbar]	Plasma Power [W]	Growth time [min]
SP512	5×5	800	2.0	150	60
SP513-2	5×5	800	2.0	120	120
SP516	5×5	800	2.0	120	60
SP520	5×5	800	2.0	150	80
SP528	5×5	800	2.0	120	120
SP529	5×5	800	2.0	120	60
SP531	5×5	800	2.0	120	27
SP533	5×5	800	2.0	120	90

4.1.3 Stoichiometry of the as-prepared samples

Although RF-sputtering is known to yield an almost perfect stoichiometry, in practice the stoichiometry is influenced by many factors during sample growth, e.g. the magnitude of plasma power, gas atmosphere, the erosion or flatness of the target etc. Therefore, it is necessary to confirm the actual stoichiometry of the sample after deposition.

Rutherford Backscattering Spectroscopy (RBS) is a powerful method to determine the depth profile of the chemical composition of thin film samples. The measurement shown here were performed at HZDR in Dresden by Dr. Lei Cao. A He²⁺ beam is incident perpendicular to the sample surface and the counts of Helium ions at different energies being backscattered from the

sample are recorded during the measurement. On the one hand, the energy of the backscattered He particles depends on the mass of the scattering atoms as well as the collision depth. On the other hand, the yield of the particles reveals the depth resolved concentration of the elements in the sample.

As shown in **Figure 4.2**, the characteristic features for some elements are marked. The simulation result shows that the stoichiometry of the system is $\text{La}_{0.716}\text{Sr}_{0.281}\text{MnO}_{3.15}$, which is close to the expected one, i.e. $\text{La}_{0.7}\text{Sr}_{0.3}\text{MnO}_3$.

Here it needs to be mentioned that the oxygen stoichiometry cannot be precisely obtained from RBS measurements since the scattering cross section for light elements is very small. Moreover, the flat terrace like feature for each element indicates that the thin film has very good quality and that all elements are distributed homogeneously inside the film.

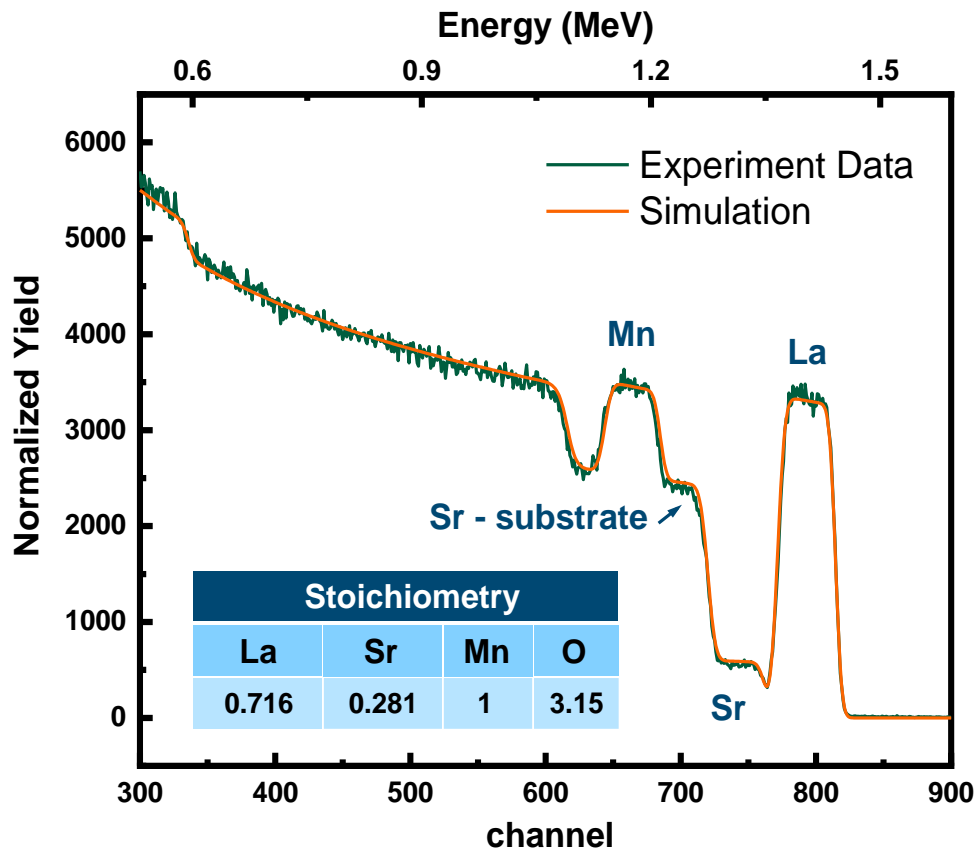


Figure 4.2 RBS spectrum with the simulated curve for the chemical stoichiometry of the as-prepared $\text{La}_{0.7}\text{Sr}_{0.3}\text{MnO}_3$ thin film grown on STO substrate. (Simulated curve using the SIMNRA software.)

4.2 Thickness dependent physical properties change on LSMO thin films

The physical properties of the LSMO thin film are strongly related to the film thickness. Therefore, a series of samples grown at 120W plasma power but with different growth times are investigated. The thickness is obtained using GenX software from XRR measurements, the errors given by the GenX software for all the samples are quite small and unreasonable, therefore, 0.1nm is taken as the error for the thickness. As shown in **Figure 4.3**, a nearly linear relationship between the growth time and the film thickness is found. Hence, at 120W the growth rate is about 40nm per hour.

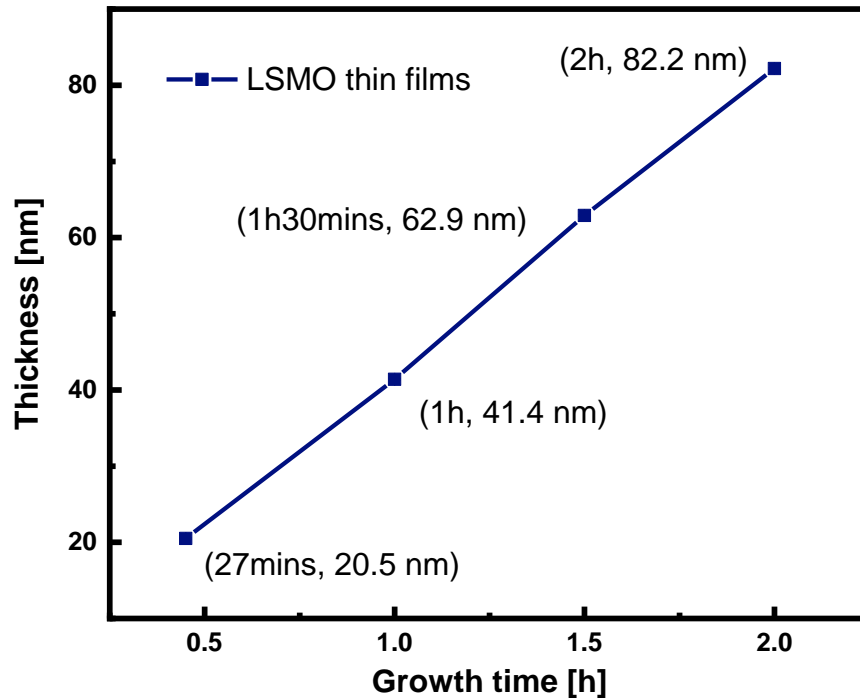


Figure 4.3 Relationship between growth time and thickness of LSMO thin film samples. The film thickness is obtained by XRR fitting using the GenX software.

4.2.1 Structure

After film preparation the X-ray diffraction scan around the (002) Bragg peak is performed on a Bruker AXS. As shown in **Figure 4.4**, the LSMO (002) Bragg peaks for different film thicknesses are located at around 47.14° without obvious shifts. The width of the peaks reflects the thickness of the LSMO films. The sharp peak and the clear thickness oscillations indicate that films show a very good crystallinity.

With a Gaussian fit, the out-of-plane lattice parameter can be directly determined via the LSMO (002) peak position. For the as-prepared state, the out-of-plane lattice parameter is $(3.852 \pm 0.001) \text{ \AA}$.

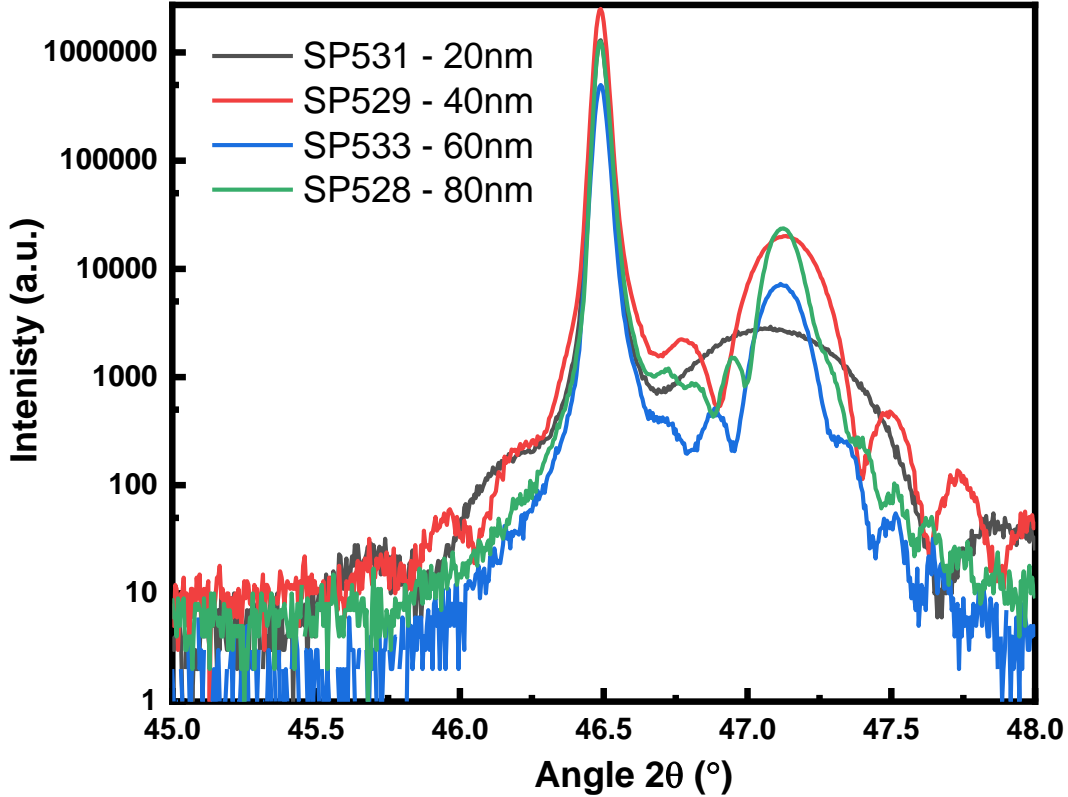


Figure 4.4 X-ray diffraction $\omega - 2\theta$ scans around the (002) Bragg peak of LSMO thin film samples with different thicknesses.

4.2.2 Magnetization

Figure 4.5 shows the magnetic behavior of a series of samples with different thickness. The magnetization vs. magnetic field curve is shown in **Figure 4.5(a)** and temperature dependent magnetization curve is plotted in **Figure 4.5(b)**. All the samples show typical ferromagnetic behavior with similar saturation magnetization, coercive field and Curie temperature, which indicates that all the samples are in very good quality and the magnetic properties are only weakly thickness dependent. The relationship between thickness and saturated magnetization is plotted in **Figure 4.6**, the small deviation of the saturation magnetization is probably due to the defects in the crystal. Normally thinner sample has more defects, thus a decrease of saturation magnetization

can be observed. With increase of growth time and thickness, the thin film quality becomes better and an increase of saturation magnetization can be obtained.

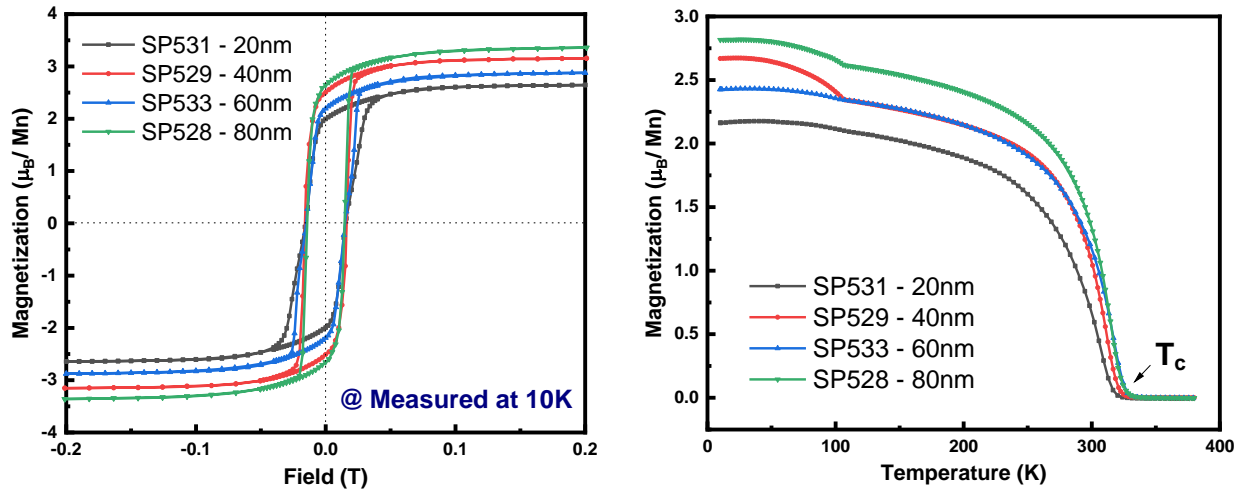


Figure 4.5 (a) Hysteresis loops of LSMO thin films with different thicknesses measured at 10K. (b) Temperature dependent magnetization curves measured at 0.01T applied field.

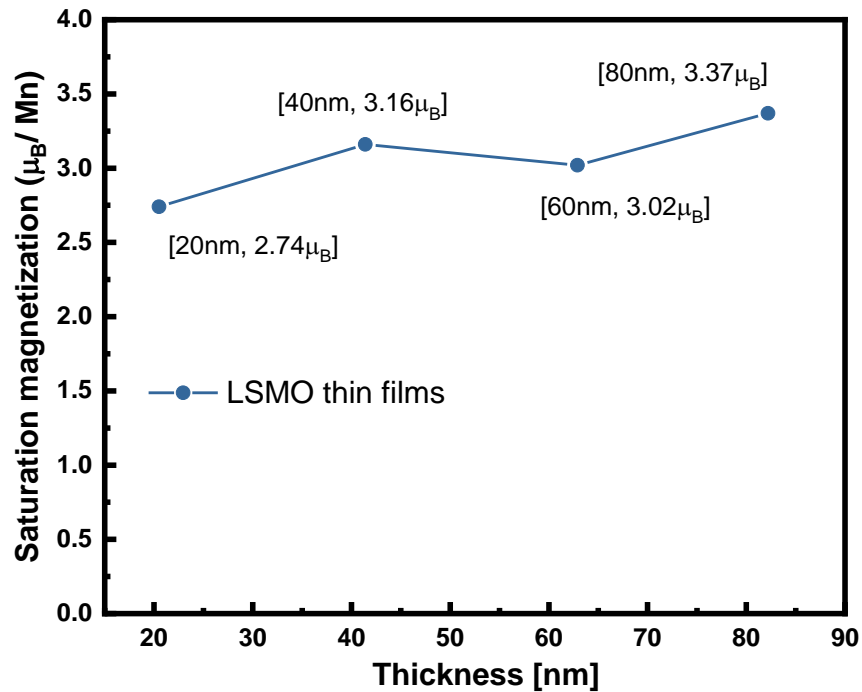


Figure 4.6 Thickness dependent magnetization curve of LSMO thin films grown on HOPSA.

4.2.3 Mean Field Theory Approximation fitting for as-prepared sample

Figure 4.7 shows the temperature dependent magnetization for a ferromagnet modeled by the mean-field theory (MFT), assuming that all the spins experience the identical average exchange field produced by all the neighbors, which is proportional to the magnetization.

Since there is no consensus for a literature value for the total angular momentum quantum number of LSMO, in this modeling a weighted average value is assumed. In LSMO the magnetization is contributed by the Mn ions. Therefore, $\text{La}_{0.7}\text{Sr}_{0.3}\text{MnO}_3$ can be considered as 30% Sr doped LaMnO_3 , thus with 70% Mn^{3+} and 30% Mn^{4+} ions. Mn^{4+} ion has an electron configuration of $3d^3$, the total orbital quantum number is $L = 2$ and total spin orbital quantum number being $S = 3 \times 1/2 = 3/2$, thus $J = |L - S| = 3/2$. The electron configuration of Mn^{3+} ions is $3d^4$, thus the total orbital quantum number is $L = 2$ while total spin orbital quantum number is $S = 4 \times 1/2 = 2$, thus $J = |L - S| = 0$. However, for 3d ions the crystal field is stronger than the spin-orbital coupling, resulting in the splitting of the 3d orbitals. Also, so-called orbital quenching is assumed. Thus, $J = 2 \times 0.7 + 3/2 \times 0.3 = 1.85$ is first considered in this modeling.

Table 4.2 shows the parameters used for the Mean-Field Theory fitting.

Table 4.2 The parameters used for MFT Fitting

L	S	J	g_J	λ	$M_s [\mu_B]$	$T_c [K]$
0	1.85	1.85	2	105.18	2.43	325.8
0	0.8	0.8	2	166.54	2.43	325.8
0	0.01	0.01	2	296.80	2.43	325.8

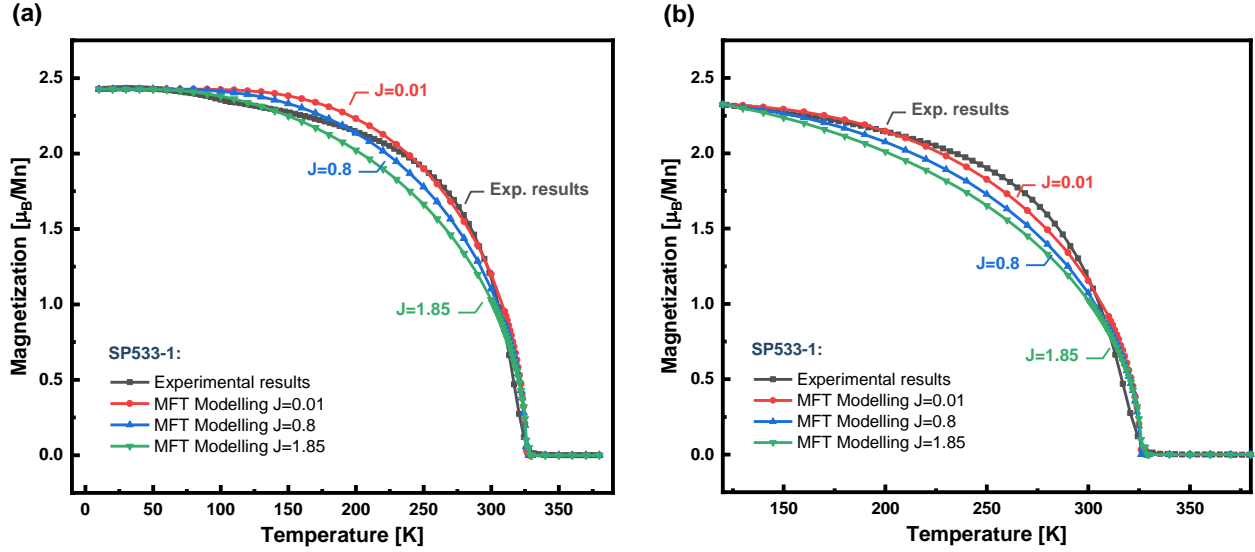


Figure 4.7 Magnetization vs. temperature curve based on MFT and experimental curve. (a) Complete curves from 10K-380K. (b) Part from 120K above the phase transition of the STO substrate at 105K.

Figure 4.7(a) shows the temperature dependent magnetization (M vs. T) curve of the experimental results and the MFA modeling in the range of 10K to 380K. Since at 105K the STO substrate experiences a phase transition, the M vs. T curve is cut below 120K to have a better comparison of the theory and real results as shown in **Figure 4.7(b)**. It is clear that the as-prepared LSMO system shows a typical ferromagnetic M vs. T behavior similar to mean field theory. Near the Curie temperature, the order parameter M decreases rapidly to nearly zero, which also corresponds to MFT. However, at temperatures smaller than T_c , the experimental order parameter of the as-prepared sample is larger than the MFA modeling, which indicates that the model values chosen in the model equation differ from the real values, e.g. the total angular momentum quantum number J . Therefore, different J -values are chosen to investigate the influence of J -values onto the MFT fitting with the fixed Curie temperature. As shown in **Figure 4.7(a)**, the fitting curve is raised up with decrease of J -value. Surprisingly, the model with $J = 0.01$ fits the experimental results at middle range temperature better, however, it is unreasonable and fits worse at low temperature. It is substantiated that a MFT fit cannot model LSMO reasonably well which is probably due to the complex electronic correlations in such systems and the J -value in complex oxides systems is complex and difficult to estimate.

In addition, the spontaneous magnetization of the model reaches zero more rapidly, while in the experiment a smoother curve is observed, which is very likely due to thermal fluctuations near T_c , which is ignored in the MFA.

4.2.4 Polarized Neutron Reflectometry on as-prepared system

In addition, polarized neutron reflectometry (PNR) measurements are performed to determine the chemical structure and magnetization for the as-prepared sample. In the model, the LSMO thin film is comprised of one top surface layer and one main layer, the interface layer is ignored to simplify the simulation. **Figure 4.8(a)** shows the PNR results measured at 120K. The spin up-up (R++) channel shows the sum of the nuclear and magnetization scattering length density (NSLD and MSLD), while the spin down-down (R--) channel shows the difference. Therefore, the splitting between the R++ and R-- curves indicates that the sample possesses a net magnetization at 120K. Here one needs to mention that at low Q_z , around 0.016 \AA^{-1} , the fitted curve deviates from the measured points. The reason is probably due to the low resolution of MARIA at low Q_z values.

Figure 4.8(b) shows the plots of the NSLD and MSLD of the as-prepared LSMO thin film sample. The detailed fitted parameters of the PNR measurements are listed in **Table 4.3**.

Table 4.3 Fit parameters for the PNR measurement of the as-prepared sample SP516-4.

SP516-4	Thickness [\AA]	NSLD [10^{-6} \AA^{-2}]	Magnetic Moment [μ_B]	MSLD [10^{-6} \AA^{-2}]	Roughness [\AA]
LSMO top	26.4 ± 0.3	3.819 ± 0.022	1.442 ± 0.035	0.653 ± 0.016	6.1 ± 0.3
LSMO	388.6 ± 1.4	3.840 ± 0.223	3.122 ± 0.022	1.421 ± 0.010	19.2 ± 2.1
STO	-	3.589 (fixed)	-	-	17.0 ± 1.0

Accordingly, the total magnetization of LSMO film can be calculated as

$$M_{total} = \frac{M_{LSMO} \cdot d_{LSMO} + M_{LSMO\ top} \cdot d_{LSMO\ top}}{d_{total}} = (3.015 \pm 0.024) \mu_B$$

where d_{total} is the total thickness of LSMO thin film.

The total magnetization corresponds to the magnetization measurement on SQUID ($M = 3.004 \mu_B$ at 120K at 0.5T) as shown in **Figure 4.9**. However, compared to the macroscopic magnetization measurement, the PNR measurement not only yields the magnetization but also the depth profile.

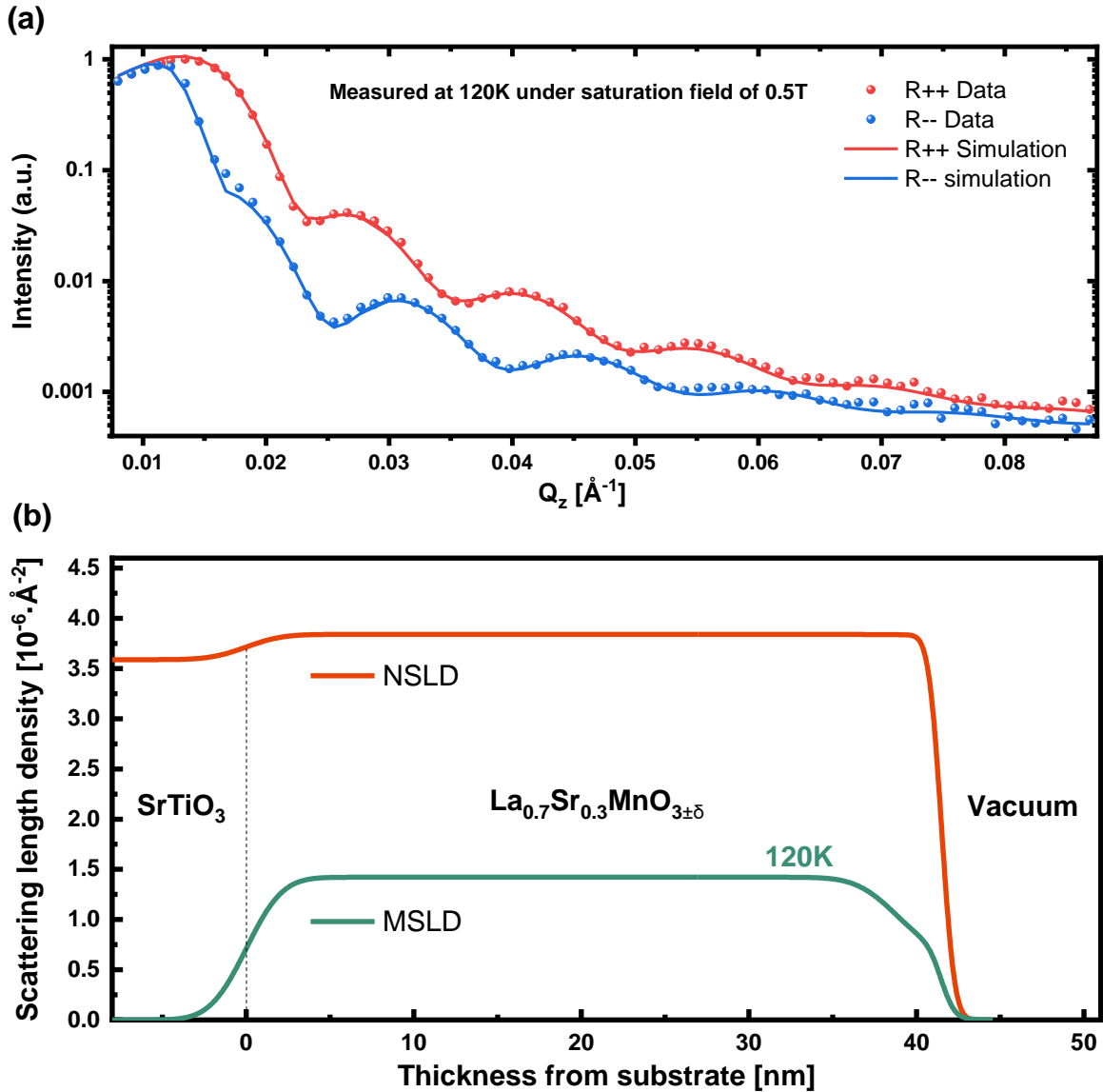


Figure 4.8 a) Polarized neutron reflectivity of the as-prepared LSMO thin film SP516-4 grown on a STO substrate, measured at 120K. The measured (symbols) and fitted (lines) curve for spin up-up (R++) and spin down-down (R--) neutrons are plotted together as a function of the scattering vector Q_z , respectively. b) Corresponding scattering length density vs. depth of the nuclear and magnetization profile, respectively.

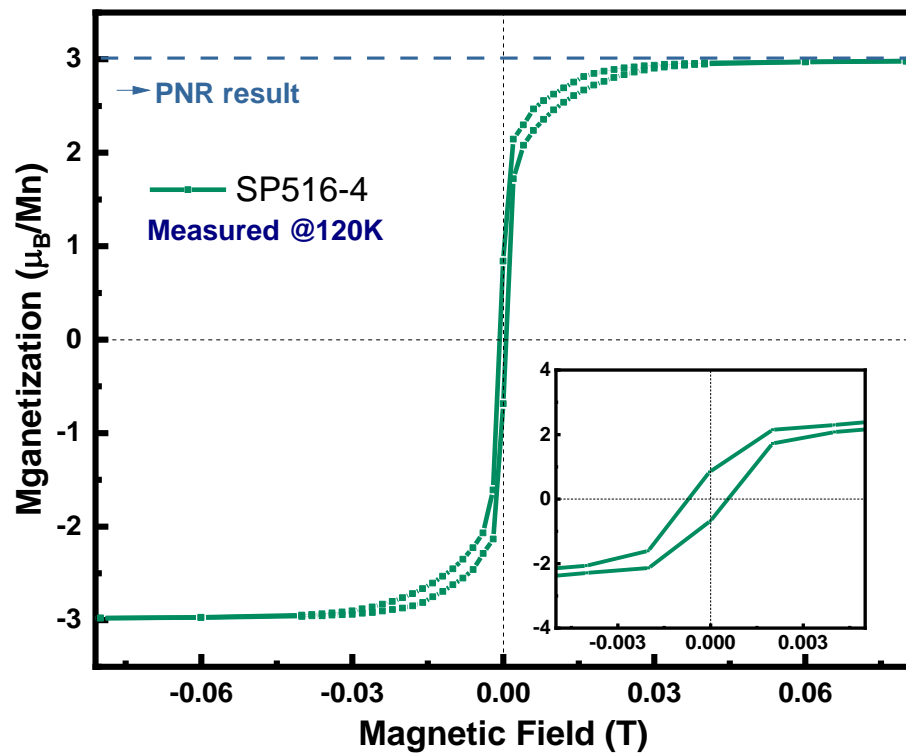


Figure 4.9 Magnetization measurement on the as-prepared sample SP516-4 at 120K.

5 Control of physical properties via topotactic phase transition on LSMO thin films by post-annealing

In this chapter, the topotactic phase transition of LSMO thin films treated at different annealing methods is investigated. In a previous study, the phase transformation from Perovskite to Brownmillerite of LSMO thin films was realized using vacuum annealing [1] and H₂ plasma treatment [42]. In this study, several new methods are performed to trigger the phase transition, i.e. post-annealing in ultra-high vacuum and aluminum assisted vacuum annealing. X-ray diffraction is employed to characterize the phase transition of the LSMO thin films. In addition, the magnetic and electronic transport properties are also investigated. Finally, the comparison of changes in structural and physical properties from different treatment methods are discussed.

5.1 Annealing methods

In order to trigger the phase transition of LSMO thin films from Perovskite to Brownmillerite, various annealing methods are performed.

- a) **Vacuum annealing in XRR chamber and OMBE chamber:** In the XRR chamber, the sample is heated directly by the sample holder up to 750°C in high vacuum (HV) of 10⁻⁶ mbar base pressure, while in the OMBE chamber the sample is heated indirectly by radiation up to 750°C in ultra-high vacuum (UHV) of 10⁻¹⁰ mbar base pressure.
- b) **Aluminum (Al) assisted vacuum annealing:** The sample is sealed together with freshly polished Aluminum foil in a quartz tube in a high vacuum of 10⁻⁵ mbar and then annealed in a furnace at various temperatures.

5.2 Structural changes induced by post-annealing

The full range XRD spectrums of LSMO thin films on STO substrate before and after post annealing are shown in **Figure 5.1**. With release of oxygen, the film peak shifts to left and finally reaches Brownmillerite phase and the superlattices emerge. The peak positions of LSMO thin films treated by HV and UHV annealing do not show obvious differences.

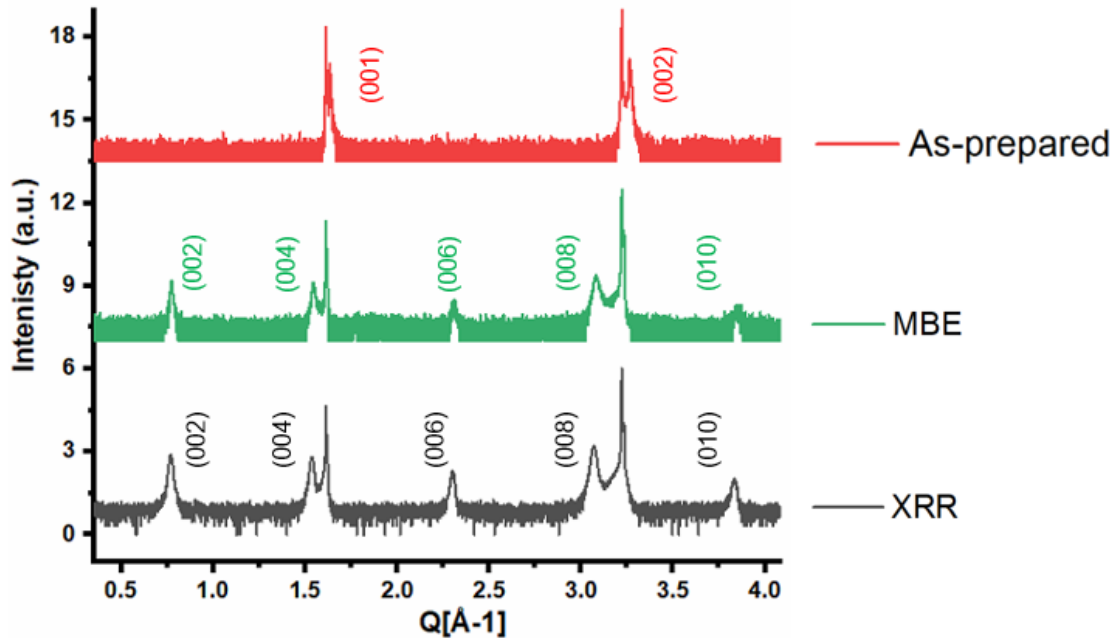


Figure 5.1 Full range X-ray diffraction patterns of $\text{La}_{0.7}\text{Sr}_{0.3}\text{MnO}_3$ thin films on STO (001) substrates before (raw) and after various post annealing methods as indicated in the figure. The peak indices are marked in the figure. As-prepared (red): PV LSMO thin film; MBE (green): After annealing in the OMBE chamber; XRR (black): After annealing in the XRR chamber.

Figure 5.2 shows the reciprocal space mapping (RSM) of the LSMO films before and after post-annealing. The RSM measurement is performed on a Bruker D8 at the institute PGI-7. The RSM of the as-prepared Perovskite films is shown in **Figure 5.2(a)**. The in-plane lattice parameter of the STO substrate is found at around 3.90 \AA , which corresponds to the literature value. The in-plane lattice parameter of LSMO is the same as STO, which indicates that the LSMO thin film is epitaxially grown on the substrate. The out-of-plane lattice constant of LSMO is around 3.85 \AA , which also corresponds well to the XRD results discussed above. As shown in **Figure 5.2(b)**, after post annealing the out-of-plane lattice parameter expands to 4.10 \AA due to release of oxygen, while the in-plane lattice constant stays the same as the substrate, indicating that the LSMO thin films are locked to the substrate without relaxation during the post annealing process.

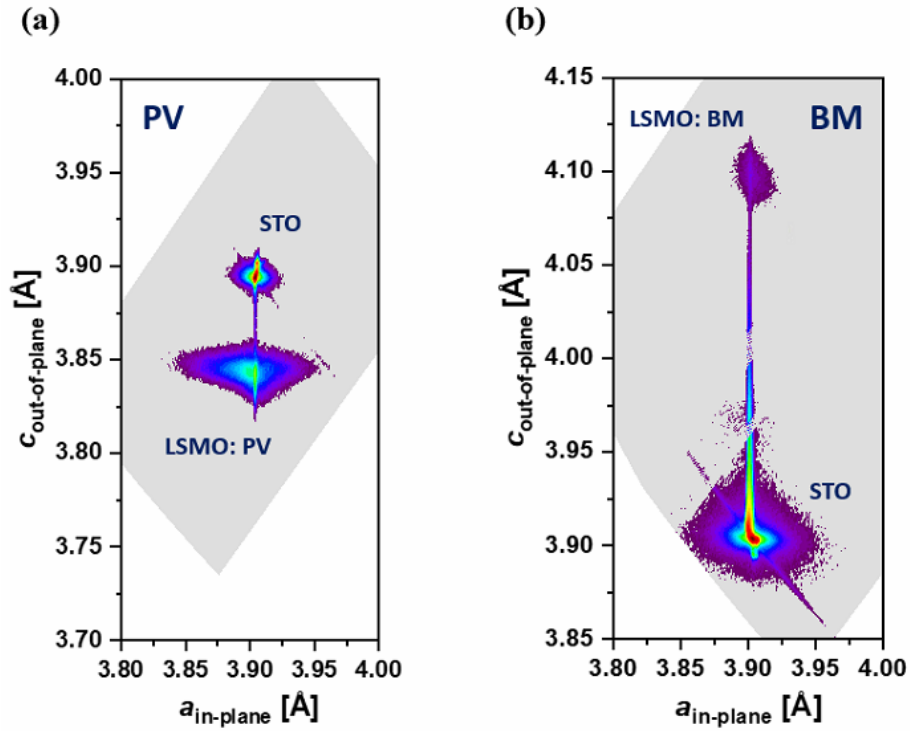


Figure 5.2 Reciprocal space mapping of the LSMO thin film samples before and after vacuum annealing. (a) As-prepared Perovskite (PV) phase and (b) after post-annealing the Brownmillerite (BM) phase.

Apart from vacuum annealing, Al-assisted annealing is also tested to trigger the phase transition. **Figure 5.3(a)** shows the experimental geometry of Al-assisted annealing on thin film. A series of temperatures are tried while using polished Aluminum as oxygen getter. As shown in **Figure 5.3(b)**, the LSMO peak disappears and the intensity of STO substrate decreases significantly after 15 hours of Al-assisted annealing at 300 °C. In order to find out the reason, RBS measurement is performed.

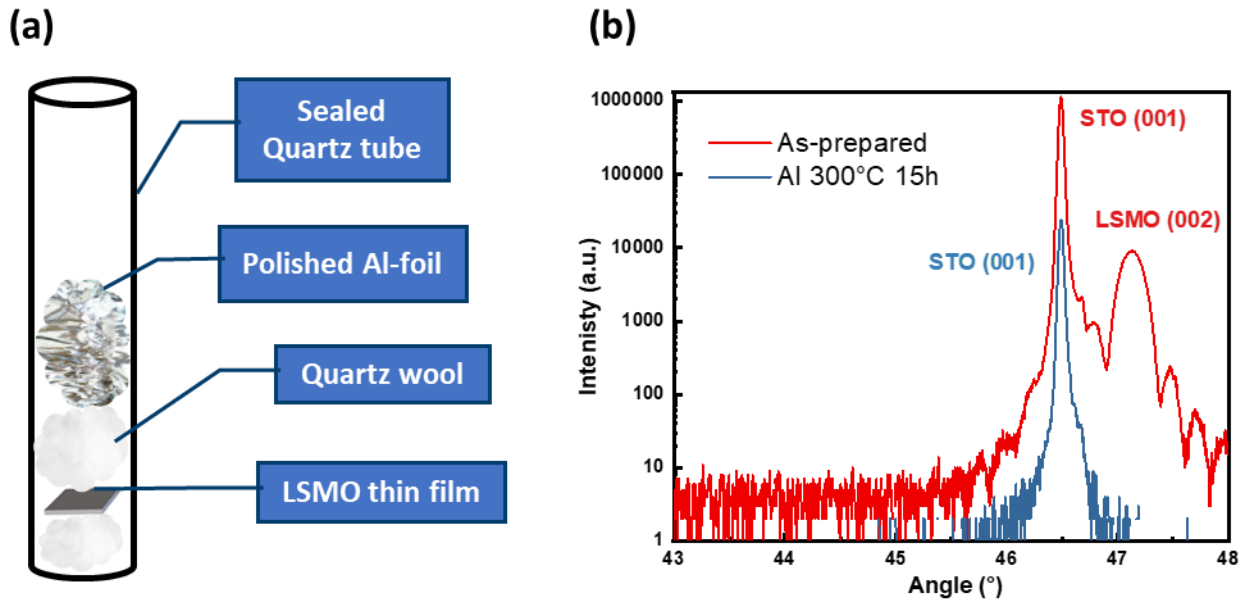


Figure 5.3 (a) Experimental geometry of polished Al-assisted annealing. (b) XRD scan around (002) of the as-prepared LSMO and after Al-assisted annealing at 300°C for 15h. The LSMO peak disappears after post-annealing.

In the RBS measurement, the channeling and random signals are plotted in **Figure 5.4**. It is clear that the intensity of Lanthanum and Strontium decreases significantly, and the characteristic terrace of Manganese disappears, which indicates the crystallographic structure of LSMO film is completely destroyed. In addition, the splitting between the channeling and random curve reveals the substrate stays crystallized. However, the slight inclination of the Sr terrace shows that the crystal lattice of the substrate is also slightly destroyed, which corresponds to the decrease of STO peak intensity in XRD spectrum as well. It shows that at 300°C the Aluminum is too efficient as getter material for thin films.

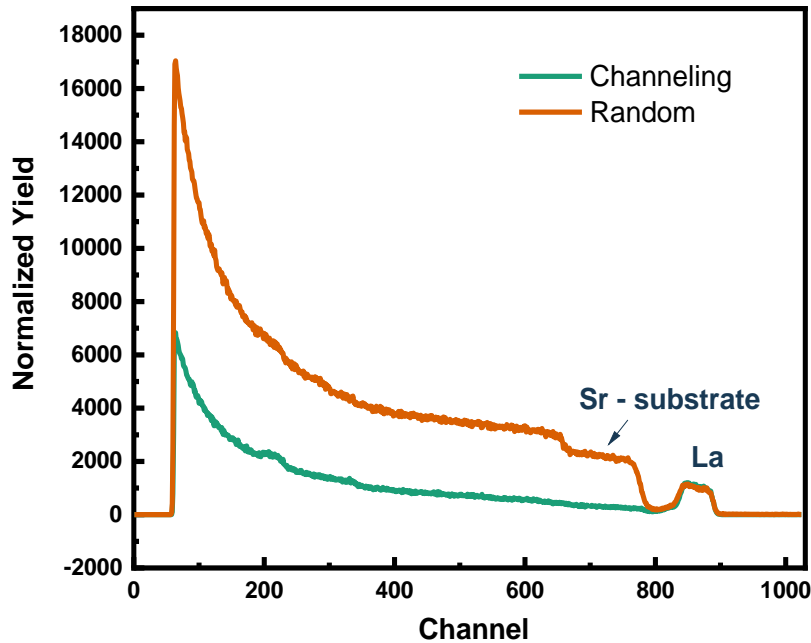


Figure 5.4 RBS spectrum of the sample treated by Aluminum assisted annealing. The brown and green curve corresponds to the channeling and random signal, respectively.

5.3 Physical property changes after post-annealing

The magnetic and electronic transport behavior of the LSMO thin films is strongly related to the exchange interactions between Mn ions. Therefore, the physical properties of the thin films are also changed simultaneously at the structural phase transition. In this section, the physical property changes after post-annealing are discussed.

5.3.1 Magnetometry

In the as-prepared state of the thin film, the ferromagnetism originates from double-exchange interactions via $\text{Mn}^{3+} - \text{O} - \text{Mn}^{4+}$ configurations. With release of oxygen, the valence state of Mn ions decreases. At some point, the Mn^{4+} ions are reduced completely to Mn^{3+} , so that the super-exchange interaction via $\text{Mn}^{3+} - \text{O} - \text{Mn}^{3+}$ configurations then dominates, and thus anti-ferromagnetism is favored. With increasing annealing time, gradually more $\text{Mn}^{2+} - \text{O} - \text{Mn}^{3+}$ configurations are achieved. Such a configuration would suggest again ferromagnetic coupling. However due to the increased distance between ions still antiferromagnetic coupling is found [43, 44].

Figure 5.5 shows the magnetization behavior of LSMO thin films before and after post-annealing. The magnetization of treated LSMO thin films drops significantly to nearly zero compared to the as-prepared ones, indicating that the Mn ions are coupled antiferromagnetically in the system. The sample treated at high vacuum annealing shows a typical anti-ferromagnetic peak with the Néel temperature around 34K, which corresponds to the previous results [1].

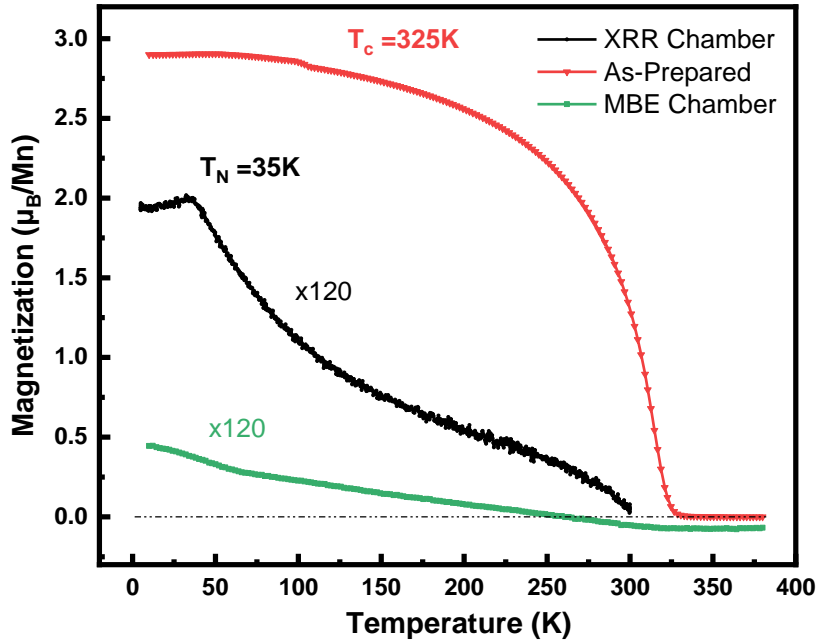


Figure 5.5 Temperature dependent magnetization curves of as-prepared sample and samples after HV and UHV annealing. The M vs. T curves of these two annealed samples are enhanced by 120 times in order to have a better comparison.

However, in this study, some unusual behavior is found in the samples annealed in ultra-high vacuum. On the one hand, the magnetization of samples treated by UHV annealing is one magnitude smaller than the sample annealed in high vacuum. On the other hand, there is no typical peak characteristic for anti-ferromagnetism. The magnetization at high temperature even drops to negative values, i.e. the diamagnetic contribution dominates.

In order to investigate the strange magnetic behavior of the sample annealed in UHV further, XMCD measurements are also employed to characterize the magnetization of the sample.

The XMCD measurements at the Mn $L_{2,3}$ edge on different state samples are shown in **Figure 5.6**. For as-prepared PV sample, it reveals a net magnetization arising from Mn ions due to double-exchange interactions. However, for the samples after HV and UHV post annealing, which are in

the BM phase, the XMCD measurements shows an extremely weak signal. This finding corresponds to the observed small macroscopic magnetization measurement as well.

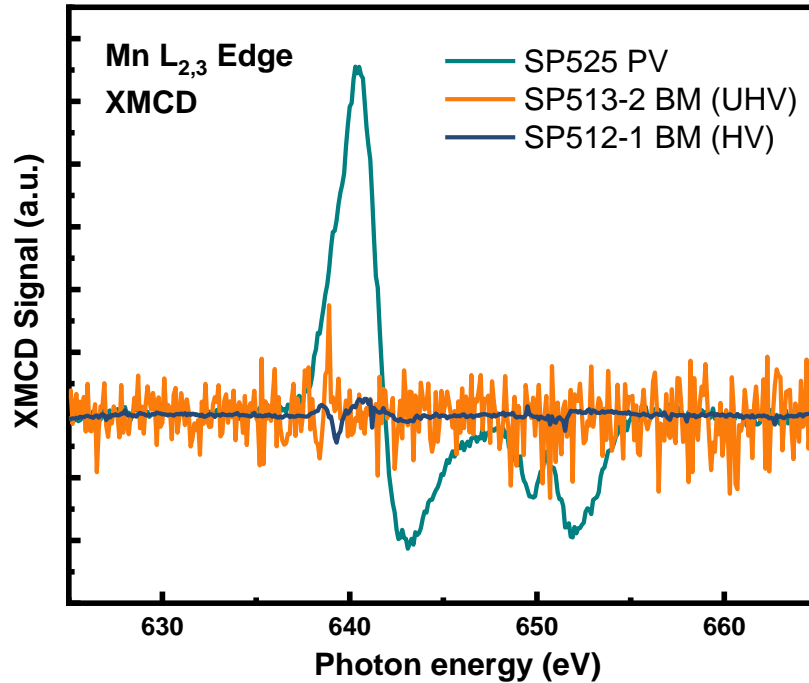


Figure 5.6 Mn XMCD spectra for LSMO/STO thin films at different annealing states.

In the LSMO system, whether it shows ferromagnetic or antiferromagnetic behavior depends on the exchange interaction between the Mn ions, which is also coupled with the valence state of Mn ions in the system. Therefore, XAS measurement is performed to investigate the valence state change before and after post-annealing.

Figure 5.7 shows the X-ray absorption spectrum for the samples in different states (at the top of the figure), the reference data for Li_2MnO_3 , Mn_2O_3 and MnO are shown below, indicating the three different valence states of Mn^{2+} , Mn^{3+} and Mn^{4+} . The data is shifted for clarity. As shown in the figure, the sample treated by HV annealing (blue curve) has more Mn^{2+} and Mn^{3+} in the system compared to the as-prepared sample (red curve), the decrease of valence state of Mn ions is due to the release of oxygen during the post annealing process. Accordingly, the $\text{Mn}^{2+} - \text{O} - \text{Mn}^{3+}$ combination dominates in the system, corresponding to anti-ferromagnetic behavior. From the spectrum, it can also be observed that there is still some Mn^{4+} left in the system. The reason is probably due to the formation of a Ruddlesden-Popper (RP) phase at the surface, which is confirmed in the previous study.

The as-prepared sample possesses also some Mn^{2+} in the system, which contradicts to the $\text{Mn}^{3+} - \text{O} - \text{Mn}^{4+}$ configuration for a PV system. An explanation is probably a surface layer on the film. From the PNR measurement (**Figure 4.8**) a decrease of magnetization on the surface is also observed.

Compared to the sample annealed in HV, the sample after UHV annealing shows an obvious increase of the Mn^{2+} peak, which corresponds to the further decrease of magnetization (**Figure 5.5**). In addition, the intensity of Mn^{3+} and Mn^{4+} peaks decrease significantly, indicating that a much purer BM phase is formed. In the previous HV annealing study, a RP phase is formed. However, in the UHV annealing, oxygen can be desorbed more easily due to the better vacuum and hence less oxygen partial pressure.

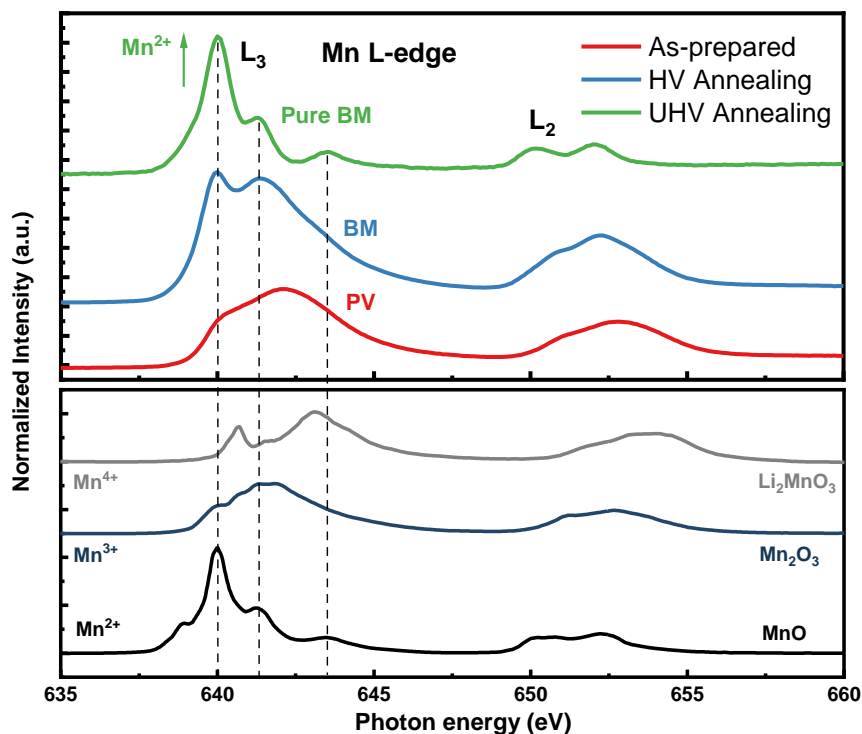


Figure 5.7 Above: X-ray absorption spectrum for the samples at different states. From bottom to top: as-prepared PV state, after HV annealing BM state and after UHV annealing BM state, respectively. Below: The reference XAS spectrum for Mn ions with different valence states in manganite. Mn reference spectra were collected at the Advanced Light Source, a U.S. DOE Office of Science User Facility under contract no. DE-AC02-05CH11231 and the data are replotted with permission from [45, 46].

5.3.2 Resistivity

In complex oxides the resistivity is very sensitive to the oxygen vacancies (defects) in the lattice and strongly coupled to the magnetic properties. Therefore, the electronic transport properties of LSMO thin films at different states is investigated to have a further comparison.

Figure 5.8(a) shows the temperature dependent resistivity of the LSMO samples in PV and BM phases. It is clear that the resistivity increases by several orders of magnitudes after post-annealing. For the as-prepared PV sample, the resistivity increases with increasing the temperature, being typical for metallic behavior. For the annealed BM samples, a decrease of resistivity is observed with the temperature increasing, which corresponds to typical insulating behavior. This indicates that the system becomes insulating during post-annealing. The resistivity for typical metal, semiconductor and insulator is $1.78 \times 10^{-6} \Omega \cdot cm$ for Cu, $10^2 \Omega \cdot cm$ for Si and $10^{14} \Omega \cdot cm$ for glass, respectively.

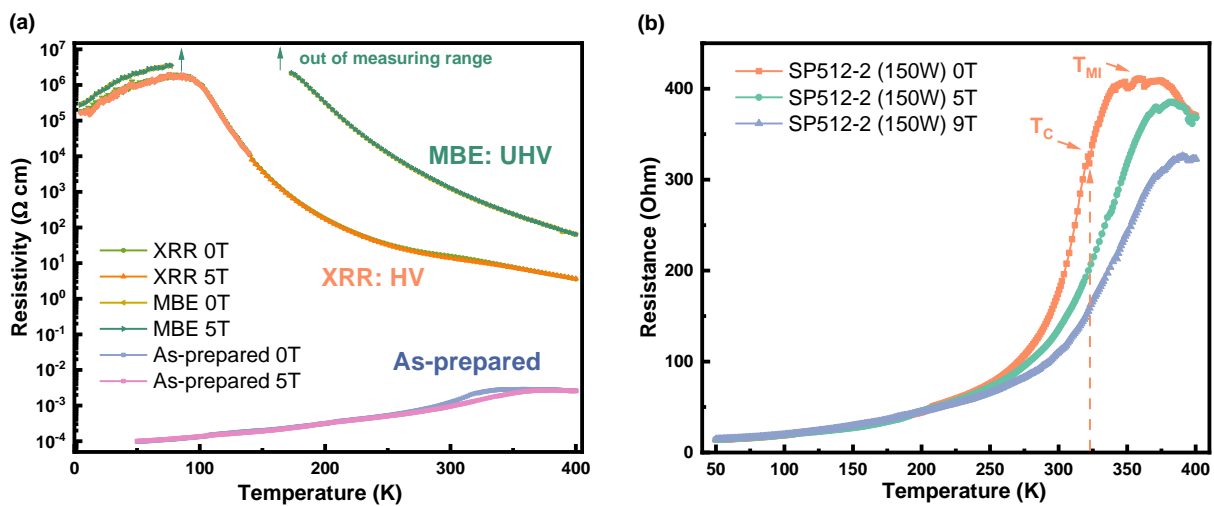


Figure 5.8 (a) Temperature dependent resistivity of the as-prepared PV phase system and after HV and UHV post annealing (BM phase). (b) Temperature dependent resistivity at various fields of the as-prepared PV film. The Curie-temperature T_C and the metal-insulator transition temperature T_{MI} are marked in the plot.

Compared to the sample annealed in HV, the sample treated by UHV annealing shows a higher resistivity due to the increase of Mn^{2+} in the system, which is consistent with the magnetic properties as well. Interestingly, both the BM samples show the transition temperature around

100K. This transition point may arise from the para- to antiferromagnetic transition. This effect will be further investigated in the future.

Moreover, the magnetoresistance vanishes in the annealed BM samples compared to the as-prepared PV sample. For better comparison, the temperature dependent resistivity at various fields measurement on the as-prepared PV film is plotted in **Figure 5.8(b)** showing a typical colossal magnetoresistance behavior.

5.3.3 Optical Property

In addition, the change of optical opacity of LSMO thin films is also observed during post-annealing. As shown in **Figure 5.9**, the as-prepared Perovskite LSMO thin film is opaque, while after post-annealing the Brownmillerite system is more transparent and the metallic luster is lost.

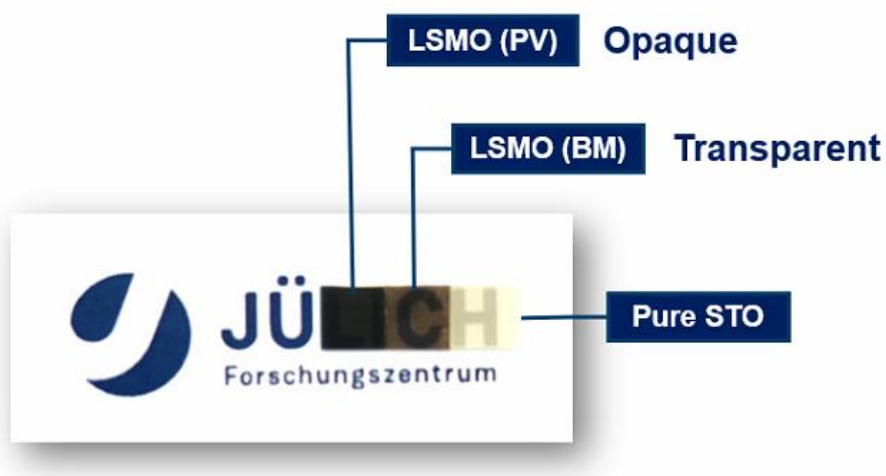


Figure 5.9 Images of different samples at different states. From left to right: Perovskite LSMO (opaque), Brownmillerite LSMO (transparent) and a pure STO substrate.

5.4 Peak oscillation phenomena during vacuum annealing

During in-situ annealing inside the XRR chamber a strange "peak oscillation" phenomenon is found. As shown in **Figure 5.10**, X-ray diffraction scans are performed from $43^\circ - 48^\circ$ manually every 6 minutes after reaching the target temperature of 750°C , in order to catch the change of the peak position of both the substrate and thin film. Then a regular scan from $43^\circ - 48^\circ$ is completed every one hour to monitor the entire phase transition process.

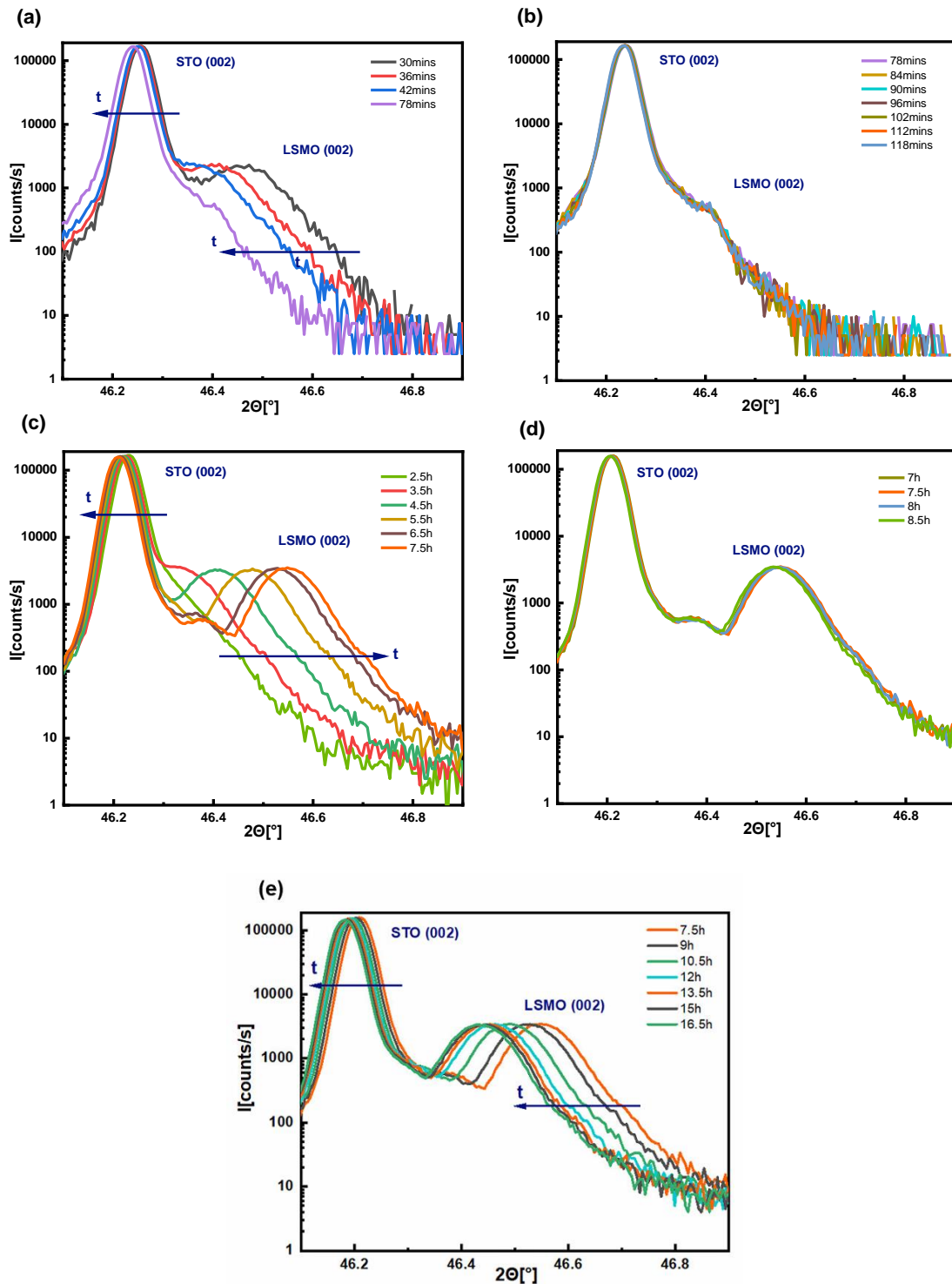


Figure 5.10 Peak Oscillation Phenomena during in-situ annealing at 750°C on sample SP520-1. (a) At the beginning, the LSMO peak shifts to the left, indicating the release of oxygen. (b) After one hour of annealing, the LSMO peak position stabilizes. (c) Then after 2.5 hours annealing the LSMO peak returns back to the right. (d) The LSMO peak stays stable again for the next 7 hours of annealing. (e) Then the LSMO peak shifts again to the left.

In the first one hour, both the LSMO and STO peaks shift to lower angles upon release of oxygen. When the LSMO peak partially overlaps with the STO peak, both peak positions remain stable for ca. 1 hour of annealing. This is followed first by a shift of the LSMO peak to the right, while the STO peak shifts to the left during several hours, then again, a period where no peak shift occurs and finally by a shift to the right again.

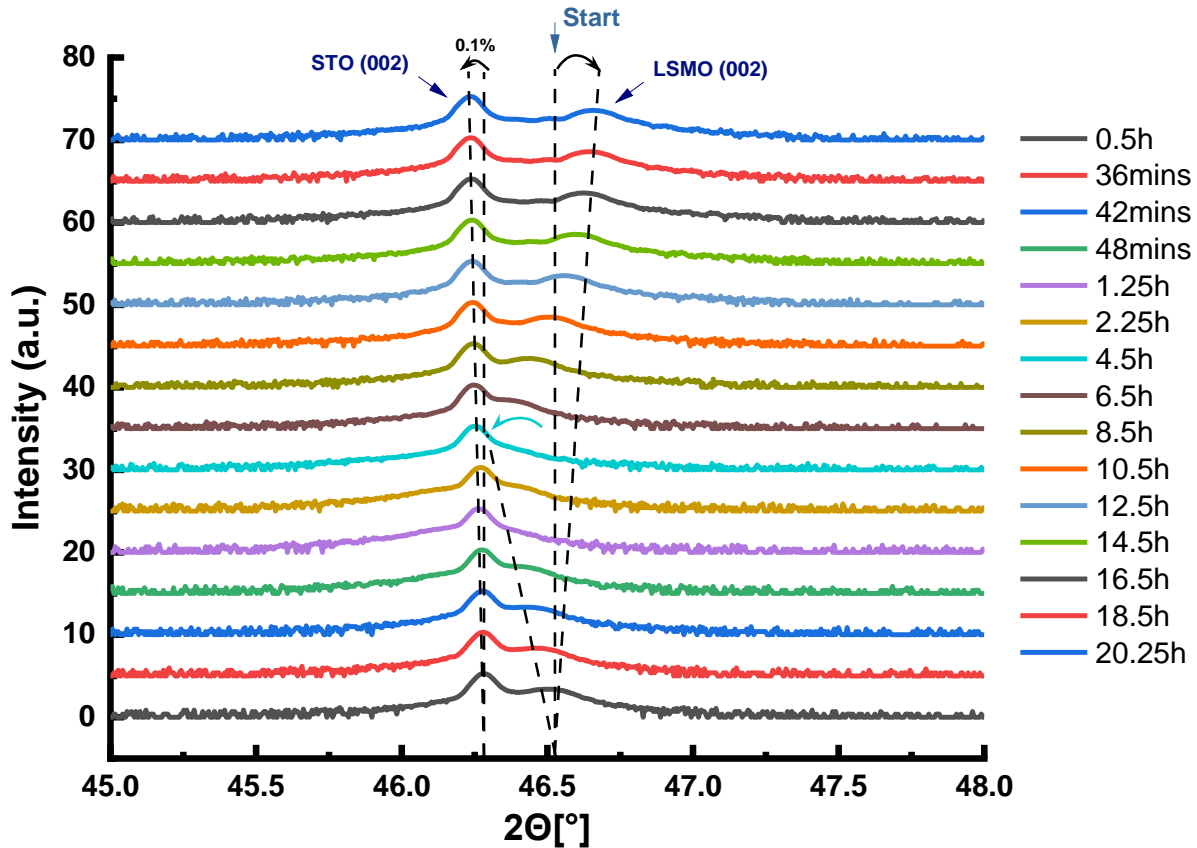


Figure 5.11 X-ray diffraction curves scanned every one hour during post-annealing at 650 degree. The change of the LSMO and STO peak positions are also marked by dashed lines.

In order to exclude possible artifacts, another annealing experiment at 650°C is performed. The peak oscillation phenomenon is also found. From **Figure 5.11** it is clear that the STO peak shifts to the left continuously with 0.1% change. However, the LSMO peak shifts first to the left and returns back to the right and even to higher angles than initially.

Because this peak oscillation phenomenon was repeated on several samples in several runs, and because the peak shift of the LSMO and STO peak occurs sometimes in different directions, an artifact e.g. due to a drift of the device is difficult to assume. Nevertheless, this finding might be due to a measurement artifact, which needs to be resolved in future studies.

A speculative physical explanation would be that the substrate STO releases oxygen during annealing and thus floods the LSMO film with oxygen and by this re-oxygenates it. This process does not occur continuously but in phases, which would explain the right-to-left oscillation. Such a scenario needs to be confirmed or falsified by future experiments.

5.5 Summary

In this chapter, various annealing methods to trigger the phase transition of LSMO thin films are discussed. The phase transition from Perovskite to Brownmillerite is successfully triggered by HV and UHV annealing. Both of them show the significant decrease of magnetization when compared to the as-prepared samples. The XMCD spectrum of Mn L-edge on the as-prepared state sample reveals strong dichroism, which indicates the PV LSMO thin film possesses a net magnetization, while for BM LSMO it shows an extremely small signal corresponding to the significant decrease of magnetization during post annealing.

However, the sample annealed by HV annealing shows a typical antiferromagnetic peak with a Néel temperature around 34K, while the sample annealed in UHV does not show a peak and even a further decrease of magnetization. This result is probably due to a further decrease of the valence state of Mn ions by introducing more oxygen vacancies. As a result, a much purer BM phase is obtained by UHV annealing. In order to investigate the spin order of these two samples, one very thick 10*10 mm² sample with a thickness of about 120nm is prepared for neutron diffraction in the future.

The electronic transport property of LSMO after post annealing is also investigated. The resistivity of the sample annealed in UHV is one order of magnitude larger than for samples treated by HV annealing.

In addition, Aluminum assisted annealing is also performed to trigger the phase transition. The LSMO thin film peak vanishes after annealing at 300°C for 15 hours from XRD. From the RBS spectrum, it is found that the thin film crystal structure is completely destroyed. It is probably due to the strong getter behavior of Aluminum. In next step, lower temperatures and shorter annealing times will be tested.

Moreover, a peak oscillation phenomenon is observed during the in-situ post annealing process. The LSMO peak shifts to left in the beginning of annealing. When the peak overlaps with the STO

peak, it shifts back to right again. After some time, it starts shifting to the left and again to the right. One possible explanation is that the LSMO thin film absorbs the oxygen released from the STO substrate, which results in the peak oscillation. This phenomenon will be investigated in the future.

6 Control of physical properties via topotactic phase transition on LSMO powders by post-annealing

This chapter introduces the systematic topotactic phase transition study on LSMO powder system. Compared to thin films, the real oxygen release process in LSMO is investigated without the influence of strain from a substrate.

6.1 Powder sample preparation

In this study, the LSMO powder sample is milled by hand from the target in the crucible for 10 minutes. After preparation, scanning electron microscopy (SEM) is used to characterize the grain sizes of the powder sample. The measurement is performed at JCNS-1. As shown in **Figure 6.1**, the hand milled LSMO powder grains have an average diameter of 2 μm .

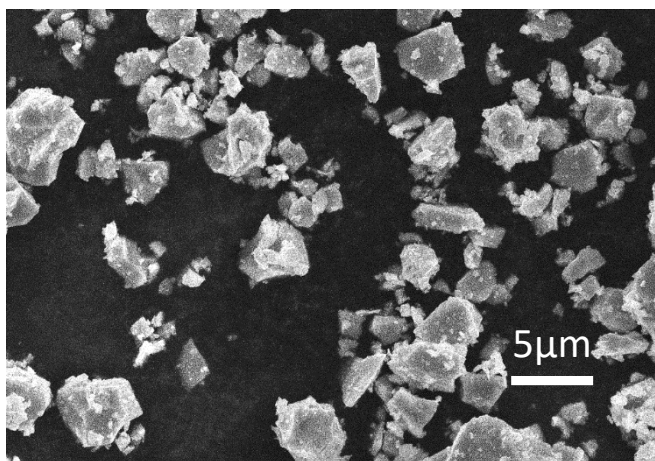


Figure 6.1 SEM image of the LSMO powder after hand-milling.

In order to trigger the phase transition process from PV to BM, the sample is annealed with polished Aluminum in a sealed quartz tube at base pressure 10^{-5} mbar. As shown in **Figure 6.2**, the LSMO powder is placed in a small quartz crucible and sealed together with some quartz wool and a freshly polished Aluminum foil. The oxygen released from LSMO is adsorbed by the Al-foil. The sealed quartz tube is heated in a furnace at 600°C for various times. After post-annealing, the structural, magnetic and electronic transport properties changes of the LSMO powder are investigated.

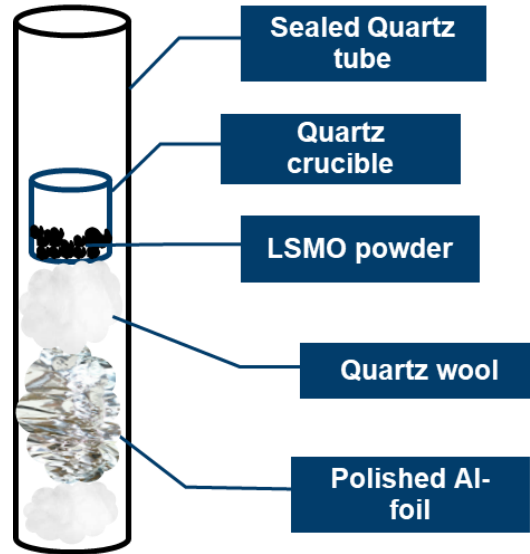


Figure 6.2 The experimental geometry of the ex-situ Aluminum assisted powder annealing in a sealed Quartz tube

6.2 Topotactic phase transition induced by Aluminum-assisted annealing

Similar with thin film, the phase transition is also observed in the powder system. As shown in **Figure 6.3**, the raw LSMO powder peaks correspond to the theoretical PV LSMO, which indicates the powder milled from LSMO target stays in good quality Perovskite phase. After 15 hours post-annealing (shown in red line), some new phases emerge (marked by arrows). With increasing the annealing time to 30 hours, some of the new peaks disappear surprisingly, but still almost all PV phase peaks remain. When increasing to 75 hours annealing, the system mostly changes to the BM phase, but still with several unknown peaks, which do not belong to either the PV or BM phase. One interesting point is that these unknown peaks emerge and then vanish and appear again during the annealing process, which might belong to intermediate phases. **Figure 6.4** shows the reference XRD spectra of some possible La, Sr, Mn- oxides during annealing. It can be found that the unknown peaks around 30° might belong to LaMnO_3 and La_2O_3 , and the peaks from 40° to 45° probably arises from LaMnO_3 , Mn_2O_3 and SrMnO_3 . The refinement of the structure will be investigated in the next step.

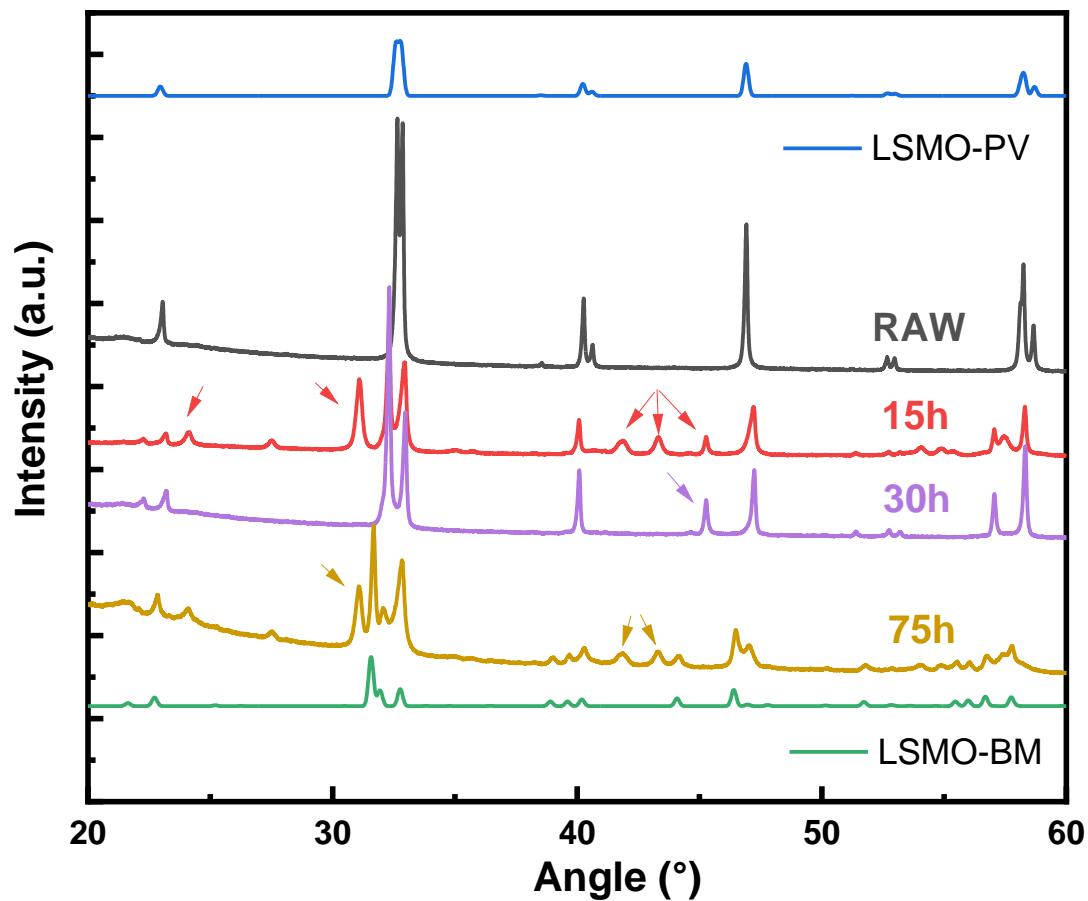


Figure 6.3 XRD spectra of LSMO powder before and after post-annealing for various times. The annealing time is marked in the figure. The theoretical XRD curve for PV (blue curve) and BM (green curve) LSMO powder samples, which are obtained from the ICSD database, are also plotted at the top and bottom.

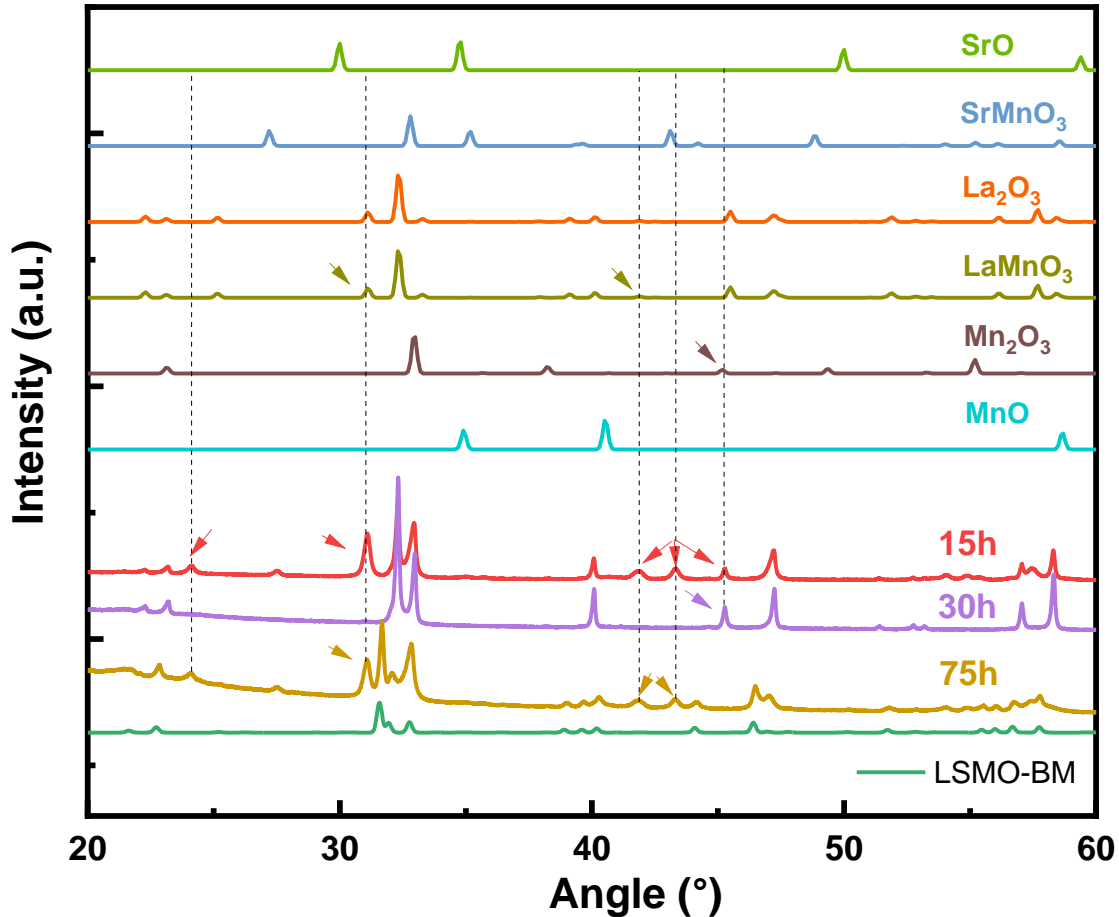


Figure 6.4 Above: reference XRD spectra of some possible La, Sr, Mn- oxides which can emerge during annealing. Below: XRD spectra of annealed LSMO powder sample after various annealing time. Some “unknown peaks” are marked by the arrow and dash lines for better comparison to the reference peaks.

6.3 Magnetic and electronic transport properties change

After post-annealing, the magnetic and electronic transport properties of the LSMO powder are measured. As shown in **Figure 6.5(a)**, the magnetization of the annealed powder decreases significantly. Comparing the magnetization of the system before and after annealing at 350K, where the contribution of an antiferromagnetic phase becomes negligible, the ratio of the amount of the ferromagnetic phase can be calculated. Only 0.4% of the ferromagnetic phase remains in the system after annealing. The small ferromagnetic contribution is due to a small PV phase left, which is also seen in the XRD spectrum.

Figure 6.5(b) shows the comparison of magnetization of the powder after 15, 30 and 75 hours annealing. With increasing annealing time, the magnetization decreases and the system turns to

anti-ferromagnetic with the Néel temperature around 50K. Moreover, the Néel temperature shifts to lower values with increasing the annealing time and another peak emerges in the powder annealed for 75 hours.

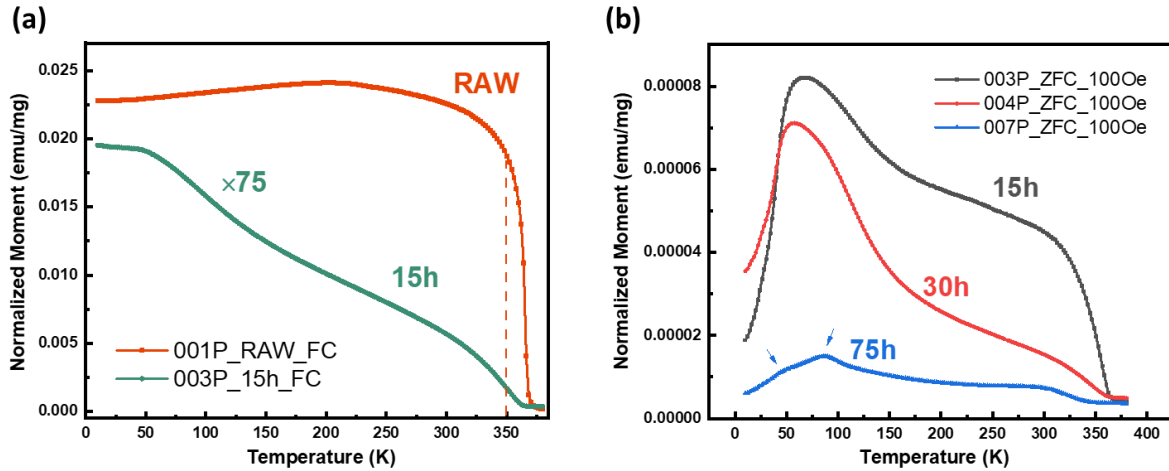


Figure 6.5 (a) Normalized magnetic moment of LSMO powder before and after 15 hours annealing. The magnetization of annealed powder sample is enhanced by 75 times to have a better comparison. (b) Comparison of magnetization for three different annealed systems after 15, 30 and 75 hours annealing.

In this study, the electrical resistance of a piece LSMO target is measured instead of loose powder.

Figure 6.6 shows the resistance of the LSMO target before and after post annealing using the 4-wire method.

By post-annealing, the resistance of the LSMO target has increased by four orders of magnitude compared to the raw system. On the other hand, the resistance of the annealed system increases with decreasing temperature which corresponds to insulating behavior. This result matches the electronic transport behavior found on the thin films. When compared to the thin film sample, both of them change from conducting to insulating behavior, while the resistance change of bulk sample is five orders of magnitude smaller than thin film sample, which is probably because a) Oxygen release process is much easier in thin film compared to bulk system. b) The bulk sample does not reach the final BM phase.

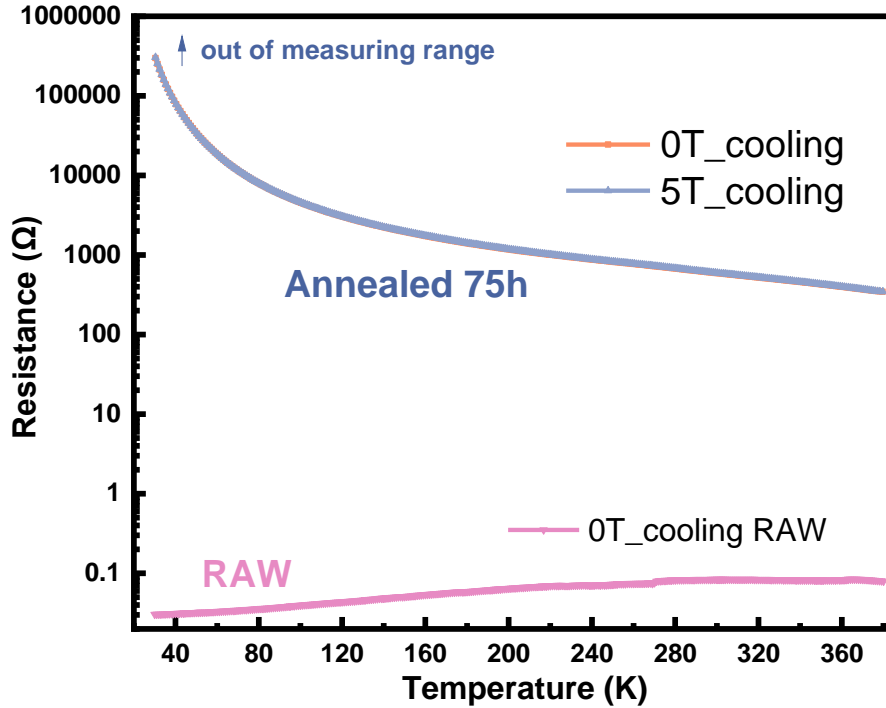


Figure 6.6 Resistance of a piece of LSMO target measured using the 4-wire method.

6.4 Summary

In this chapter, the phase transition process of LSMO powder is discussed. By means of Al-assisted annealing, some new phases emerge after 15 hours annealing but the sample mainly stays in the PV phase. With increasing the annealing time to 75 hours, all of the BM LSMO peak emerge but there are still some unknown peaks which do not belong to either the PV or BM phase. This indicates that most of the LSMO changes to the BM phase.

After post-annealing, the magnetic and electronic transport properties are investigated. The magnetization decreases significantly and most of the system changes from ferromagnetic to antiferromagnetic behavior. However, due to some residual PV and intermediate phases, ferromagnetic signatures can still be observed in the annealed system. In the future, refinement of the X-ray diffraction curves will be performed to study which phases these unknown peaks belong to.

The resistance of a piece of the LSMO target is measured before and after annealing, because it is not possible to measure the powder sample directly. The system changes to insulating behavior by post-annealing, which is consistent with the thin film results discussed above.

Summary & Outlook

This study is continuation of Lei Cao's PhD study. In the previous work, the PV to BM phase transition process of LSMO thin film is realized by High-Vacuum (HV) annealing in XRR. In this study, various annealing methods are performed to trigger the phase transition, i.e. High-Vacuum annealing in XRR; Ultra-High-Vacuum (UHV) annealing in MBE; Aluminum (Al) assisted annealing. Especially, the differences between UV and UHV annealing are discussed. In addition, the change of structural, magnetic and electronic properties of LSMO powder and bulk samples after Al-assisted annealing are investigated and compared to the thin films.

The $\text{La}_{0.7}\text{Sr}_{0.3}\text{MnO}_3$ thin films were grown on STO single crystal substrates by High Oxygen Pressure Sputter Deposition and a perfect Perovskite phase was obtained for the samples with different thicknesses from 20nm to 80nm. They have the same out-of-plane lattice parameter and a typical ferromagnetic behavior with similar coercive fields, saturation magnetizations and Curie temperatures. The Mn XMCD spectrum reveals the as-prepared LSMO sample possesses net magnetization and polarized neutron reflectivity results show that it has a net magnetization (around $3.015 \mu_B$), which is consistent with the macroscopic magnetization measurement (around $3 \mu_B$). Moreover, the temperature dependent magnetization curve of one as-prepared thin film sample is modeled by Mean-Field Theory. Near T_C the curve fits the experimental results well, however, below T_C , a large deviation is found between the modeling and the results.

After preparation, LSMO thin films are treated by various annealing methods to trigger the phase transition. I.e. Ultra-High Vacuum annealing (UHV) and Aluminum (Al) assisted annealing. The previous HV annealing method is also repeated to have a better comparison. Both samples treated by HV and UHV annealing change to the BM phase and show a significant decrease of magnetization. The Mn XMCD spectrum reveals the magnetization of samples decreases nearly to zero after annealing as well. The huge increase of resistivity in both samples also confirms the transition from a conductor to an insulator, which corresponds to a PV to BM transition. However, after HV annealing, the sample shows typical antiferromagnetic behavior with a Néel temperature around 34K. This differs from the UHV annealed sample, whose magnetization decreases even more than the sample in HV annealing. These results can be explained by the valence state changes of Mn ions. From the XAS spectrum of Mn L_3 -edge, the valence state of Mn ions decreases with

introducing oxygen vacancies by post annealing. When annealed at UHV, the composition of Mn^{2+} increases, so that a much purer BM phase was obtained, resulting in further decrease of magnetization and increase of resistivity. Why no typical para- to -antiferromagnetic transition peak in the magnetization was observed in this sample still needs to be investigated. A very thick film beyond 120 nm was prepared for studying the spin structure of the samples annealed in UHV by neutron scattering in the future.

Moreover, the thin film samples are also annealed together with polished Aluminum at 300°C for 15 hours. However, from the XRD and RBS spectra one finds that the LSMO structure is completely destroyed, indicating that this method is too strong for thin films. In the next step, lower temperatures and shorter annealing times will be tried.

In addition, the phase transition in LSMO powder is also investigated in order to study a system without the influence of strain from a substrate. After 15 and 30 hours of Al-assisted annealing, some new phases emerge but the system mostly stays in the PV phase. When increasing the annealing time to 75 hours, most of the powder transforms to the BM phase but still with some unknown phases. The magnetic and electronic transport properties also support the transition from ferro- to antiferromagnetic and from conducting to insulating behavior. The refinement of the XRD spectra will be done in the future to study what the unknown phases belong to.

Acknowledgement

Here I would like to express my sincere gratitude to following people:

Prof. Dr. Thomas Brückel for providing me the opportunity to work at JCNS-2.

Prof. Dr. Regina Dittmann for agreeing to take the role of my second examiner.

Especially, I would like to thank my supervisor **PD Dr. Oleg Petravic** for providing me this very interesting project and for the supports and discussions we had last year, and **Dr. Lei Cao** for many fruitful discussions, supports and the RBS and resistivity measurements.

Annika Stellhorn, Patrick Schöffmann, Dr. Connie Bednarski-Meinke and Tanvi Bhatnagar-Schöffmann, the MBE team, for the sample annealing and fruitful discussion.

Dr. Felix Gunkel, Moritz Weber, Suqin He and Hong Yan for the support of XRD and RSM measurements.

Dr. Alexandros Koutsoumpas and Dr. Kirill Zhernenkov for the help and discussions on PNR measurement in MLZ.

Dr. Tomas Duchon for the support and discussions on XAS and XMCD measurement at BESSY.

Dr. Ulrich Rücker for the help and support at X-ray reflectometer.

Dr. Shibabrata Nandi for the help and support at PPMS and Dynacool.

Dr. Emmanuel Kentzinger for the help and support at powder X-ray diffractometer.

Jörg Perßon for the help with sample annealing.

Berthold Schmitz, Frank Gossen for technical assistance on HOPSA, MPMS, PPMS and Dynacool.

Finally, I would like to thank all my colleagues and friends for their help and fruitful discussions and creating a so lovely atmosphere in JCNS-2.

Last but not least, I would like to thank my family and my girlfriend for their support and encouragement.

References

1. Cao, L., et al., *Reversible Control of Physical Properties via an Oxygen-Vacancy-Driven Topotactic Transition in Epitaxial $\text{La}_{0.7}\text{Sr}_{0.3}\text{MnO}_{3-\delta}$ Thin Films*. *Adv Mater*, 2019. **31**(7): p. e1806183.
2. Rose, G., *Beschreibung einiger neuen Mineralien des Urals*. *Annalen der Physik*, 1839. **124**(12): p. 551-573.
3. Peña, M.A. and J.L.G. Fierro, *Chemical Structures and Performance of Perovskite Oxides*. *Chemical Reviews*, 2001. **101**(7): p. 1981-2018.
4. Tilley, R.J.D., *The ABX_3 Perovskite Structure*, in *Perovskites*. 2016, John Wiley & Sons p. 1-41.
5. Tilley, R.J.D., *Perovskites: Structure–Property Relationships*. 2016: John Wiley & Sons.
6. Kalinin, S.V. and N.A. Spaldin, *Functional Ion Defects in Transition Metal Oxides*. *Science*, 2013. **341**(6148): p. 858-859.
7. Gunkel, F., et al., *Ordering and Phase Control in Epitaxial Double-Perovskite Catalysts for the Oxygen Evolution Reaction*. *ACS Catalysis*, 2017. **7**(10): p. 7029-7037.
8. Weber, M.L., et al., *Electrolysis of Water at Atomically Tailored Epitaxial Cobaltite Surfaces*. *Chemistry of Materials*, 2019. **31**(7): p. 2337-2346.
9. Hemberger, J., et al., *Structural, magnetic, and electrical properties of single-crystalline $\text{La}_{1-x}\text{Sr}_x\text{MnO}_3$ ($0.4 < x < 0.85$)*. *Physical Review B*, 2002. **66**(9).
10. Dixon, E., J. Hadermann, and M.A. Hayward, *Structures and Magnetism of $\text{La}_{1-x}\text{Sr}_x\text{MnO}_{3-(0.5+x)/2}$ ($0.67 \leq x \leq 1$) Phases*. *Chemistry of Materials*, 2012. **24**(8): p. 1486-1495.
11. Blundell, S., *Magnetism in Condensed Matter*. 2001: Oxford University Press, 2001.
12. Howard, C.J. and H.T. Stokes, *Group-Theoretical Analysis of Octahedral Tilting in Perovskites*. *Acta Crystallographica Section B*, 1998. **54**(6): p. 782-789.
13. Woodward, P.M., et al., *Influence of Cation Size on the Structural Features of $\text{Ln}_{1/2}\text{A}_{1/2}\text{MnO}_3$ Perovskites at Room Temperature*. *Chemistry of Materials*, 1998. **10**(11): p. 3652-3665.
14. Anderson, P.W., *Antiferromagnetism. Theory of Superexchange Interaction*. *Physical Review*, 1950. **79**(2): p. 350-356.
15. Heisenberg, W., *Zur Theorie des Ferromagnetismus*. *Zeitschrift für Physik*, 1928. **49**(9): p. 619-636.
16. Guirado-López, R.A., J. Dorantes-Dávila, and G.M. Pastor, *Orbital Magnetism in Transition-Metal Clusters: From Hund's Rules to Bulk Quenching*. *Physical Review Letters*, 2003. **90**(22): p. 226402.
17. Thompson, A.G., *MOCVD technology for semiconductors*. *Materials Letters*, 1997. **30**(4): p. 255-263.

18. Mitra, P., A.P. Chatterjee, and H.S. Maiti, *ZnO thin film sensor*. Materials Letters, 1998. **35**(1): p. 33-38.
19. Green, M.A., *Thin-film solar cells: review of materials, technologies and commercial status*. Journal of Materials Science: Materials in Electronics, 2007. **18**(1): p. 15-19.
20. Reichelt, K., *Nucleation and growth of thin films*. Vacuum, 1988. **38**(12): p. 1083-1099.
21. Venables, J.A., *Atomic processes in crystal growth*. Surface Science, 1994. **299-300**: p. 798-817.
22. Brückel, T., Richter, D., Roth, G., Wischnewski, A. and Zorn. R., *Neutron Scattering*. 2015: Forschungszentrum Jülich GmbH.
23. Cao, L., *Controlling structural and physical properties of epitaxial transition metal oxide films through oxygen stoichiometry*, PhD thesis. 2019, Forschungszentrum Jülich GmbH, RWTH Aachen.
24. Norton, C.S.G., *X-Ray Diffraction: A practical approach*. 1998: Springer Science+Business Media, LLC
25. Zabel, H., *X-ray and neutron reflectivity analysis of thin films and superlattices*. Applied Physics A, 1994. **58**(3): p. 159-168.
26. Gibaud, J.D., *X-ray and Neutron Reflectivity*. Principles and Applications. 2009.
27. Mussler, G., *X-ray Diffraction of Semiconductor Heterostructures: Jülich Spring School 2020*. 2020.
28. *Application of polarized neutron reflectometry to studies of artificially structured magnetic materials*, in *Modern Techniques for Characterizing Magnetic Materials*, Y. Zhu, Editor. 2005, Springer US: Boston, MA. p. 107-155.
29. Waschk, M., *Interface Phenomena in $La_{1/3}Sr_{2/3}FeO_3$ and $La_{2/3}Sr_{1/3}MnO_3$ heterostructures and a quest for p-electron magnetism*, PhD Thesis 2017, Forschungszentrum Jülich GmbH, RWTH Aachen.
30. M. I. Faley, U.P., R. Speen, and R. E. Dunin-Borkowski, *High oxygen pressure deposition and patterning methods for metal oxide heterostructures*. 2012.
31. Schmitz, M., *Strain and electric field mediated manipulation of magnetism in $La_{(1-x)}Sr_xMnO_3/BaTiO_3$ heterostructures*. 2015, Forschungszentrum Jülich GmbH, RWTH Aachen
32. *Quantum Design, Physical Property Measurement System: User's Manual (Quantum Design, Inc., San Diego, CA, 2002)*.
33. PAUW, L.J.v.d., *A method of measuring specific resistivity and hall effect of discs of arbitrary shape*, in *Semiconductor Devices: Pioneering Papers*. p. 174-182.
34. Mattauch, S., et al., *The high-intensity reflectometer of the Julich Centre for Neutron Science: MARIA*. J Appl Crystallogr, 2018. **51**(Pt 3): p. 646-654.
35. *Heinz Maier-Leibnitz Zentrum et al. (2015). MARIA: Magnetic reflectometer with high incident angle. Journal of large-scale research facilities, 1, A8. <http://dx.doi.org/10.17815/jlsrf-1-29>.*

36. https://www.helmholtz-berlin.de/forschung/oe/fg/mi-synchrotron-adiation/synchrotron/x-ray/x-ray-absorption/index_en.html.
37. Deng, J., et al., *Large lattice mismatch effects on the epitaxial growth and magnetic properties of FePt films*. Journal of Magnetism and Magnetic Materials, 2018. **446**: p. 125-134.
38. Lan, F., et al., *Observing a previously hidden structural-phase transition onset through heteroepitaxial cap response*. Proceedings of the National Academy of Sciences, 2019. **116**(10): p. 4141-4146.
39. Lebedev, O.I., et al., *Structure and properties of artificial $[(La_{0.7}Sr_{0.3}MnO_3)_m(SrTiO_3)_n]_{15}$ superlattices on (001) $SrTiO_3$* . Journal of Applied Physics, 2003. **94**(12): p. 7646-7656.
40. Adamo, C., et al., *Enhanced electrical and magnetic properties in $La_{0.7}Sr_{0.3}MnO_3$ thin films deposited on $CaTiO_3$ -buffered silicon substrates*. APL Materials, 2015. **3**(6): p. 062504.
41. Kawasaki, M., et al., *Atomic Control of the $SrTiO_3$ Crystal Surface*. Science, 1994. **266**(5190): p. 1540-1542.
42. Chen, S., et al., *Versatile and Highly Efficient Controls of Reversible Topotactic Metal–Insulator Transitions through Proton Intercalation*. Advanced Functional Materials, 2019. **29**(50): p. 1907072.
43. Goodenough, J.B., *Theory of the Role of Covalence in the Perovskite-Type Manganites*. Physical Review, 1955. **100**(2): p. 564-573.
44. Kanamori, J., *Superexchange interaction and symmetry properties of electron orbitals*. Journal of Physics and Chemistry of Solids, 1959. **10**(2): p. 87-98.
45. Li, Q., et al., *Quantitative probe of the transition metal redox in battery electrodes through soft x-ray absorption spectroscopy*. Journal of Physics D: Applied Physics, 2016. **49**(41): p. 413003.
46. Qiao, R., et al., *Spectroscopic fingerprints of valence and spin states in manganese oxides and fluorides*. Current Applied Physics, 2013. **13**(3): p. 544-548.